Uplift Histories of Africa and Australia From Linear Inverse Modeling of Drainage Inventories

John F. Rudge[1], Gareth G. Roberts[2], Nicky White[1], Christopher N.

Richardson[3]

———

Corresponding authors: G. G. Roberts, Department of Earth Science and Engineering, Imperial

College London, SW7 2AZ, UK (gareth.roberts@imperial.ac.uk).

N. White, Bullard Laboratories, Madingley Rise, Madingley Road, Cambridge, CB3 0EZ, UK

(njw10@cam.ac.uk).

[1]Bullard Laboratories, Department of

Earth Science, University of Cambridge,

UK.

[2]Department of Earth Science and

Engineering, Imperial College London, UK.

[3]BP Institute, Bullard Laboratories,

University of Cambridge, UK.

Abstract.   We describe and apply a linear inverse model which calculates spatial and temporal patterns of uplift rate by minimizing the misfit between inventories of observed and predicted longitudinal river profiles. Our approach builds upon a more general, non-linear, optimization model, which suggests that shapes of river profiles are dominantly controlled by upstream advection of kinematic waves of incision produced by spatial and temporal changes in regional uplift rate. Here, we use the method of characteristics to solve a version of this problem. A damped, non-negative, least squares approach is developed that permits river profiles to be inverted as a function of uplift rate. An important benefit of a linearized treatment is low computational cost. We have tested our algorithm by inverting 957 river profiles from both Africa and Australia. For each continent, the drainage network was constructed from a digital elevation model. The fidelity of river profiles extracted from this network was carefully checked using satellite imagery. River profiles were inverted many times to systematically investigate the trade-off between model misfit and smoothness. Spatial and temporal patterns of both uplift rate and cumulative uplift were calibrated using independent geologic and geophysical observations. Uplift patterns suggest that the topography of Africa and Australia grew in Cenozoic times. Inverse modeling of large inventories of river profiles demonstrates that drainage networks contain coherent signals that record the regional growth of elevation.

1. Introduction

Uplift and denudation of the Earth's surface are responses to different tectonic and sub-plate processes. Conversely, spatial and temporal patterns of uplift rates indirectly contain useful information about these processes. In the continents, considerable effort has been expended to constrain these rates by exploiting a range of techniques. For example, databases of uplift, rock cooling and river incision rates have been built using radiometric dating of emergent marine terraces, (U-Th)/He thermochronometry, clumped-isotope altimetry, optically-stimulated luminescence and the history of sedimentary flux [see, e.g., *Tanaka et al.*, 1997; *Ghosh et al.*, 2006; *Flowers et al.*, 2008; *Galloway et al.*, 2011; *Pedoja et al.*, 2011]. From a global perspective, these databases comprise spot measurements which means that spatial coverage can be limited. In most continents, drainage networks set the pace of denudation [e.g. *Anderson and Anderson*, 2010]. Since these networks are widespread, the notion of combining a quantitative understanding of drainage development with independent calibration is an attractive one. It may be possible to determine spatial and temporal patterns of regional uplift rate, which in turn could improve our understanding of tectonic and sub-plate processes.

Here, we show how linear inverse modeling of longitudinal river profiles, with appropriate calibration, may help to determine uplift rate histories. *Pritchard et al.* [2009] and *Roberts & White* [2010] first showed that individual river profiles can be inverted by varying uplift rate as a function of time. Subsequently, *Roberts et al.* [2012] developed a non-linear optimization model which fits inventories of river profiles as a function of the spatial and temporal pattern of uplift rate. Their general methodology has several important

advantages. For example, the relative significance of advective and diffusive erosional processes can be explored, precipitation rate can be varied through time and space, and *Monte Carlo* inverse modeling can be used to investigate how variations and uncertainties in erosional parameters affect patterns of calculated uplift rate.

A justifiably simpler modeling strategy is amenable to linearization, which greatly speeds up the optimization process [*Pritchard et al.*, 2009; *Goren et al.*, 2014; *Fox et al.*, 2014]. This strategy has two significant benefits. First, the erosional parameter space can be more thoroughly and consistently explored. Secondly, it becomes more practicable to interrogate large drainage inventories on a continent-wide basis. We develop a damped, non-negative, least squares algorithm and apply it to drainage inventories from Africa and Australia. This algorithm is motivated by the results of our earlier analysis which exploited non-linear optimization techniques [e.g. *Paul et al.*, 2014; *Czarnota et al.*, 2014]. It permits assessment of the applicability of the stream power erosional model at a range of spatial and temporal scales. *Goren et al.* [2014] and *Fox et al.* [2014] have also developed a linear inverse model, which differs in terms of both implementation and application.

2. Modeling Strategy

It is generally agreed that the shape of a longitudinal river profile (i.e. elevation, z, as a function of upstream distance, x) is determined by some combination of uplift rate, U, and erosion rate, E, both of which can vary as a function of time and space. Thus

$$-\frac{\partial z}{\partial t} = E(x,t) + U(x,t) \tag{1}$$

where x is distance from the river mouth and t is time before present day. *Roberts &*

White [2010] showed that if the shape of a river profile is known, it is feasible to invert for

uplift rate as a function of time and/or space. The crux of this problem lies in knowing

the erosional history of a river. Erosion of a river channel is a complex process, which is

usually approximated by assuming that two forms of erosion occur. The first form assumes

that elevation along a river profile is controlled by headward propagation of steep slopes

[i.e. detachment-limited erosion; *Howard & Kerby*, 1983; *Whipple & Tucker*, 1999]. The

second form assumes that elevation is strongly influenced by sedimentary transport [i.e.

transport-limited erosion; *Sklar & Dietrich*, 1998, 2001; *Rosenbloom & Anderson*, 1994;

Whipple & Tucker, 2002; *Tomkin et al.*, 2003].

Erosion rate can be written as

$$E(x,t) = -v_\circ[PA(x)]^m \left(\frac{\partial z}{\partial x}\right)^n + \kappa(x)\frac{\partial^2 z}{\partial x^2} \qquad (2)$$

where $v_\circ$ is a calibration constant with the dimensions of velocity if $m = 0$, P is precipi-

tation rate which can vary with space and time, A is upstream drainage area that can be

measured at the present day, m and n are dimensionless erosional constants whose values

are much debated, and κ is 'erosional diffusivity', which could vary along a river profile.

In a series of contributions, *Pritchard et al.* [2009], *Roberts & White* [2010], *Roberts*

et al. [2012] and *Paul et al.* [2014] showed that the general inverse model can be posed

and solved. They demonstrated that values of the four erosional parameters, $v_\circ$, m, n

and κ, affect residual misfits between observed and predicted river profiles in different

ways. There is considerable debate about the values of $v_\circ$, m, and in particular n [e.g.

van der Beek & Bishop, 2003; *Roberts et al.*, 2012; *Royden & Perron*, 2013; *Mudd et al.*,

2014; *Lague*, 2014]. In general, $v_\circ$ determines the timescale for knickpoint retreat and

its value must be independently estimated from geologic constraints (e.g. present-day measurements of incision). Both *Roberts & White* [2010] and *Croissant and Braun* [2014] showed that v_o and m trade off negatively with each other so that different combinations of v_o and m yield equally acceptable fits between observed and predicted river profiles.

The value of n is subject to much discussion (see, e.g., *Lague*, 2014). Solutions of the detachment-limited model (i.e. first term on right-hand side of Equation 2) can develop shocks if $n > 1$ so that steeper slopes propagate faster than shallower slopes [*Pritchard et al.*, 2009; *Royden & Perron*, 2013]. If shocks develop, steep slopes can consume shallower slopes and part of the uplift history will be erased, resulting in spatio-temporal gaps. If $n = 1$, the advective velocity is $v_o(PA)^m$ and uplift events map directly into changes of elevation. There is no convincing evidence for shock-wave behavior which implies that $n = 1$ [*Pritchard et al.*, 2009]. A more compelling argument is given by *Paul et al.* [2014] who examined residual misfits between observed and predicted river profiles as a function of n. They showed that global minima occur at, or near, $n = 1$. These minima exist for different model regularizations and for different degrees of smoothing, suggesting that drainage inventories are poorly fitted when $n \neq 1$. Their results are consistent with some field studies, which imply that $n \sim 1$ [e.g. *Whittaker et. al.*, 2007; *Whittaker and Boulton*, 2012].

Figure 1 shows the results of jointly inverting the Orange river and its longest tributaries that drain South Africa using the non-linear inverse method of *Roberts et al.* [2012]. During each inversion run, v_o and n were co-varied to test the sensitivity of calculated uplift to changes in the value of erosional parameters [see *Paul et al.*, 2014]. The residual root-mean-squared (rms) misfit, H, between observed and predicted river profiles is given

111   by

$$H = \sqrt{\frac{1}{K} \sum_{i,j=1}^{I,J} \left(\frac{z_{ij}^o - z_{ij}^c}{\sigma} \right)^2} \qquad (3)$$

113   where z_{ij}^o and z_{ij}^c are observed and predicted river profile elevations, σ is the uncertainty

114   associated with each elevation (typically ~ 20 m away from narrow channels; *Farr et al.*,

115   2007), I is the number of points along a given river profile, J is the number of river

116   profiles, and K is total number of data points. Figure 1d shows that the rms misfit has

117   a global minimum at $n \sim 1$. At $n = 1$, a reliable uplift rate history can be retrieved. If

118    $n < 1$, we found that the calculated peak uplift rate is higher and later. If $n > 1$, the

119   calculated peak uplift rate is both smaller and earlier, in agreement with the finding of

120   *Goren et al.* [2014]. For example if $n = 0.7$, calculated peak uplift rate shifts forward

121   to ~ 9 Ma. If $n = 1.5$, the calculated peak uplift rate shifts backward to ~ 40 Ma.

122   Figure 1f–h shows how residual misfit varies as a function of erosional parameters for a

123   set of forward models where $U(t)$ is fixed. Note that a global minimum occurs at $n = 1$,

124   although some trade-off between v, m and n occurs. Combined with previously published

125   results, these analyses suggest that it is reasonable to assume $n \sim 1$, which then justifies

126   a linear inverse approach.

127   *Rosenbloom & Anderson* [1994] have suggested that κ is unlikely to be greater than

128   5×10^5 m^2 Ma^{-1}. Nevertheless, it is possible that κ varies by many orders of magnitude

129   (e.g. $1-10^7$ m^2 Ma^{-1}). In our inverse models, river profiles are sampled every 10–20

130   km, which implies that the minimum value of κ that can be resolved is 10^7 m^2 Ma^{-1}

131   (i.e. $\kappa = l^2/T_l$, where $l =$ horizontal resolution and $T_l =$ longevity of a river). This

132   value exceeds all reported estimates and implies that 'erosional diffusivity' can be safely

133   ignored. In other words, advective retreat of uplift signal is the dominant control and

134   transport-limited processes are of negligible importance at the scales under consideration

135   [e.g. *Berlin and Anderson*, 2007].

136   Finally, a parsimonious strategy assumes that both A, P and the reference level (i.e. sea

137   level) are invariant. In fact, A is undoubtedly modified by river capture events and pre-

138   cipitation rates vary with space and time. The integral solution of Equation (1) suggests

139   that significant temporal changes of A and P have a relatively minor effect on calculated

140   uplift histories. Changes in A scale time, which is clear from the governing equation when

141   diffusion is neglected. Since it is taken to a fractional power, A can vary by $\pm 0.5A$ without

142   adversely affecting calculated uplift rate histories. *Paul et al.* [2014] showed that their

143   African results are essentially unchanged when precipitation rate is varied, provided P

144   varies with a period of less than ~ 10 Ma. They also showed that lithology and slope,

145   curvature or steepness index correlate less well at wavelengths greater than several kilo-

146   meters and that drainage planforms have probably been configured by Neogene dynamic

147   support. *Czarnota et al.* [2014] showed that altering river profile lengths by 10–50 km

148   has a small effect on calculated uplift rate histories. Finally, it can be shown that rapid

149   glacio-eustatic changes in sea level do not adversely affect the long wavelength component

150   of river profiles [e.g. *Miller et al.*, 2005].

151   A key outcome of earlier optimization schemes, which solve Equation (1) in its general

152   form, is that erosional parameter values must be constrained using independent obser-

153   vations of uplift and/or incision rate histories. Without careful calibration, uplift rate

154   histories cannot be convincingly determined [e.g. *Royden & Perron*, 2013]. In some loca-

155   tions (e.g. southeast Australia; Colorado Plateau; West Africa), local uplift and incision

156   histories demonstrate how $v_\circ$, m and n trade off against each other [*Stock & Montgomery*,

157 1999; *Czarnota et al.*, 2014]. Since our previous results are insensitive to published values

158 of κ and since $n \sim 1$ gives the best fit to data, we can now formulate the linear inverse

159 problem.

3. A Linear Inverse Model

3.1. Method of Characteristics

160 Our experience of solving the general optimization problem suggests that the evolving

161 shape of a river profile can be approximated by

$$-\frac{\partial z}{\partial t} + vA^m \frac{\partial z}{\partial x} = U(x, t). \tag{4}$$

163 This kinematic wave equation can be solved using the well-known method of characteristics

164 [e.g. *Lighthill & Whitham*, 1955; *Weissel and Seidl*, 1998]. The solution takes the form

165 of $z(x, t) = z(x(t), t)$. Since

$$\frac{\mathrm{d}z}{\mathrm{d}t} = \frac{\partial z}{\partial t} + \frac{\mathrm{d}x}{\mathrm{d}t}\frac{\partial z}{\partial x} = \left(vA^m + \frac{\mathrm{d}x}{\mathrm{d}t}\right)\frac{\partial z}{\partial x} - U(x(t), t), \tag{5}$$

167 the solution can be written as a pair of ordinary differential equations

$$\frac{\mathrm{d}x}{\mathrm{d}t} = -vA^m, \tag{6}$$

$$\frac{\mathrm{d}z}{\mathrm{d}t} = -U(x(t), t). \tag{7}$$

171 Appropriate boundary conditions are

$$x = x^*, \, z = z^* \text{ at } t = 0, \tag{8}$$

$$\text{and } x = 0, \, z = 0 \text{ at } t = \tau_G. \tag{9}$$

175 The first boundary condition represents the present day, where at a position x^* along a

176 river, the elevation is z^*. τ_G is termed the Gilbert Time for position x^*. The second

177 boundary condition represents a time in the past, τ_G, at which the characteristic curve

178 intersects the river mouth (i.e. $x = 0$) which occurs at sea level (i.e. $z = 0$). From

179 Equations (6), (8), and (9), the Gilbert Time must satisfy

$$\tau_G = \int_0^{x^*} \frac{\mathrm{d}x}{vA^m}. \tag{10}$$

181 A general solution for Equations (6)–(9) can be written in integral form as

$$\tau_G - t = \int_0^{x(t)} \frac{\mathrm{d}x}{vA^m}, \tag{11}$$

$$z^* = \int_0^{\tau_G} U(x(t), t)\,\mathrm{d}t. \tag{12}$$

185 This analysis closely follows the approaches used by *Lighthill & Whitham* [1955], *Luke*

186 [1972], *Weissel and Seidl* [1998], *Smith et al.* [2000] and *Pritchard et al.* [2009].

3.2. Linear Least Squares Inversion

187 We wish to use a collection of observations, z^*, to invert the integral Equation (12) for

188 uplift rate, $U(x, t)$. First, the problem must be discretized in both space and time. Spatial

189 discretization is accomplished by using a triangular mesh of the domain. Temporal dis-

190 cretization is accomplished by using a finite set of time intervals. In this way, uplift values

191 can then be specified at a discrete set of spatial and temporal nodes as a vector of values

192 given by $\mathbf{U}$. Values of uplift between these nodes are obtained by linear interpolation.

193 Given a discrete set of positions, x^*, and the upstream drainage area, A, along a river

194 profile, Equation (10) can be straightforwardly integrated using the trapezoidal rule. This

195 integration yields values of Gilbert Time. Equation (11) is then used to obtain the charac-

196 teristic curves. These curves are combined with linear interpolation to discretize Equation

197 (12), once again using the trapezoidal rule. The resultant matrix equation takes the form

$$\mathbf{z} = \mathrm{M}\mathbf{U} \tag{13}$$

199 for a set of elevations, $\mathbf{z}$, at different positions on different river profiles (Appendix A).

We can now invert Equation (13) to find $\mathbf{U}$ from $\mathbf{z}$. To avoid the possibility of positive and negative oscillations, a non-negativity constraint is normally imposed [*Parker*, 1994]. Since this particular problem is often under-determined (i.e. M can have fewer rows than columns), it is also necessary to exploit a damped least squares approach. We minimize

$$|\mathbf{MU} - \mathbf{z}|^2 + \lambda_S^2 |\mathbf{SU}|^2 + \lambda_T^2 |\mathbf{TU}|^2$$

$$\text{subject to } \mathbf{U} \geq 0, \tag{14}$$

which is a non-negative least squares (NNLS) problem. λ_S and λ_T are smoothing parameters, which control the regularisation of this problem. The matrix S represents spatial smoothing and is given by

$$|\mathbf{SU}|^2 = \int_S \int_{t=0}^{t_{\max}} |\nabla U|^2 \, dt \, dS. \tag{15}$$

Matrix T represents temporal smoothing and is given by

$$|\mathbf{TU}|^2 = \int_S \int_{t=0}^{t_{\max}} \left| \frac{\partial U}{\partial t} \right|^2 \, dt \, dS. \tag{16}$$

λ_S and λ_T are chosen by analyzing the trade-off between smoothness and misfit [*Parker*, 1994]. We solve this NNLS problem using a limited memory version of the Broyden-Fletcher-Goldfarb-Shanno algorithm, L-BFGS-B, which is suited to problems with large sparse matrices [e.g. *Broyden et al.*, 1973]. We successfully benchmarked our results by implementing the slower active set algorithm of *Lawson & Hanson* [1987], which always converges optimally since it fulfils the Karush-Kuhn-Tucker conditions [e.g. *Kuhn and Tucker*, 1951]. In practise, computational cost is reduced by a factor of $\sim 10^4$ compared to non-linear optimization methods [e.g. *Roberts et al.*, 2012].

Goren et al. [2014] and *Fox et al.* [2014] describe an alternative linear least squares algorithm that exploits an empirical Bayesian approach. In their algorithm, a prior model

₂₂₃ of the uplift history is first selected. This prior model uses a guess of the average uplift

₂₂₄ rate based upon channel elevation and upstream drainage area observations (see paragraph

₂₂₅ following Equation (21) on page six of *Goren et al.*, 2014). Then, by updating this prior

₂₂₆ model with the observations, a posterior model is calculated. This posterior model stays

₂₂₇ close to the prior model and thus inherits some of its attributes. *Goren et al.* [2014] do

₂₂₈ not explicitly damp temporal gradients of uplift rate. Instead, they damp departures

₂₂₉ from their prior model by setting the value of Γ, the damping parameter. If $\Gamma \rightarrow \infty$,

₂₃₀ the posterior model converges toward the prior model (see their Equation 21). *Goren et*

₂₃₁ *al.* [2014] damp the spatial gradients of uplift rate by imposing a functional form on the

₂₃₂ spatial variation of uplift rate. In contrast, *Fox et al.* [2014] deliberately choose not to

₂₃₃ damp temporal gradients of uplift rate. They damp spatial gradients of uplift rate by

₂₃₄ specifying a correlation length scale parameter for their prior model. *Goren et al.* [2014]

₂₃₅ and *Fox et al.* [2014] show best-fit solutions which have residual misfits of up to ± 150 m

₂₃₆ and ± 500 m, respectively.

4. Examples

4.1. Uplift as Function of Time

₂₃₇ The linear inversion model can be used to fit a single river profile by allowing uplift

₂₃₈ rate to vary as a function of time alone. In southern Africa, there is excellent geologic

₂₃₉ and geophysical evidence for Neogene uplift of a series of three domes with diameters

₂₄₀ of $\sim$ 1000 km [*Giresse et al.*, 1984; *Burke*, 1996; *Partridge*, 1998; *Jackson et al.*, 2005;

₂₄₁ *Burke and Gunnell*, 2008; *Al-Hajri et al.*, 2009]. A history of rapid uplift is constrained

₂₄₂ by emergent Plio-Pleistocene marine terraces, which suggest that in places modern uplift

₂₄₃ rates along the coastline exceed 0.3 mm/a [*Giresse et al.*, 1984; *Partridge & Maud*, 1987;

Partridge, 1998; *Guiraud et al.*, 2010]. Offshore, erosional truncation of deltaic foreset deposits records 0.5–1 km of post-Pliocene (i.e. 5.3–0 Ma) uplift as well as an older Oligo-Miocene (25–30 Ma) uplift event [*Al-Hajri et al.*, 2009]. Uplift histories can be used to calibrate the values of v and m [*Roberts & White*, 2010].

The South African dome is drained to the west by the Orange catchment, to the east by the Limpopo catchment, and to the south by a set of short, steep rivers [*Partridge*, 1998]. Figure 1b apparently shows differences in Gilbert time across drainage divides in South Africa, which have been interpreted as evidence that drainage divides migrate [*Willett et al.*, 2014]. It is difficult to resolve behavior at the head of a river since it represents a singularity and so juxtaposed Gilbert time discrepancies may be artefacts. *Roberts & White* [2010] showed that these southward draining rivers have prominent knickzones and so are highly disequilibrated. Previous inverse modeling suggests that several phases of Neogene uplift have occurred. In Figure 2, the Orange river has been inverted using erosional parameter values of $v = 3.62$ and $m = 0.35$ [*Paul et al.*, 2014]. These values were constrained using Miocene to present-day uplift rates [*Partridge*, 1998; *Partridge & Maud*, 2000; *Burke and Gunnell*, 2008]. Note that if A is rewritten as $A/A_\circ$, where $A_\circ$ is the maximum upstream area, v has the dimensions of velocity.

Bearing in mind that uplift is permitted to vary as a function of time alone, our results suggest that peak uplift rates occurred between 20 Ma and the present day at rates which exceed 0.05 mm/a. The tail of cumulative uplift between 80 and 20 Ma is a consequence of assuming that uplift rate does not spatially vary. The results of linearized inversion are compatible with those obtained by *Pritchard et al.* [2009], *Roberts & White* [2010] and *Paul et al.* [2014].

4.2. Uplift as Function of Time and Space

Regional uplift varies as a function of time and space, which means that modeling individual river profiles by varying uplift rate as a function of time alone is of limited practical use. Furthermore, a single profile on its own cannot be used to determine the spatial variation of uplift rate. However, *Roberts et al.* [2012] showed that large inventories of river profiles could be jointly inverted by varying uplift through time and space. The linear inverse model can be used in a similar way. Here, we show how continent-wide inventories of river profiles can be used, subject to appropriate calibration, to determine the spatial and temporal pattern of uplift of large regions. We chose to analyze Africa and Australia, which have previously been modeled using a general optimization approach [*Paul et al.*, 2014; *Czarnota et al.*, 2014].

4.2.1. Africa

The African continent is surrounded by passive margins [*Burke*, 1996]. Its physiography is strongly bimodal: sub-equatorial Africa is characterized by a broad $\sim 10^4 \times 10^4$ km superswell; northern Africa is generally low-lying. Superimposed on this bimodal framework are smaller $\sim 1000 \times 1000$ km domal swells [e.g. *Holmes*, 1944; Figure 3]. The oldest oceanic lithosphere that abuts the African continent has residual depths of a few hundred meters [*Winterbourne et al.*, 2014]. These depth anomalies suggest that the domal swells intersecting the margins of Africa are dynamically supported by 100s of meters [Figure 3a]. Onshore, admittance studies of the relationship between gravity and topography suggest that the 'egg-box' physiography of Africa is a response to the pattern of convective circulation beneath the plate [e.g. *Jones et al.*, 2012]. Simulations of mantle convection suggest that dynamic topography grew rapidly during the last 30 million years [e.g. *Gur-*

nis et al., 2000; Moucha & Forte, 2011]. However, these simulations fail to predict the present-day basin and swell morphology of African topography. Three lines of evidence indicate that prior to ~ 35 Ma the African continent was low-lying. First, the distribution of post-Albian marine deposits shows that large portions of north and east Africa were below sea level [e.g. Sahagian, 1988; Figure 3c]. Secondly, Paleogene laterites and lateritic gravels indicate that topographic gradients were low [Burke and Gunnell, 2008]. Finally, carbonate reef deposits fringed several African deltas in Paleogene times, which is consistent with negligible clastic efflux [Figure 3c]. Since Oligocene times, sedimentary flux to Africa's deltas has dramatically increased, there has been widespread basaltic magmatism, and peneplains have been warped [e.g. Burke, 1996; Partridge, 1998; Walford et al., 2005; Figure 3d]. Here, we jointly invert an inventory of river profiles to estimate the spatial and temporal pattern of topographic growth.

704 river profiles were extracted from a 3 arc second ($\sim 90 \times 90$ m) SRTM digital elevation model using ESRI flow routing algorithms. Rivers which drain domal swells (e.g. Bié, Namibia, Southern Africa) form radial patterns (Figure 3a). Their longitudinal profiles are strongly convex upward. Broad knickzones occur, which are tens of kilometers long and hundreds of meters high and traverse different lithologies. In contrast, profiles of rivers draining North African swells (e.g. Hoggar, Tibesti, Afar) are smoothly concave upward (Figure 4).

Most African river profiles can be accurately fitted (Figure 4). The largest discrepancies are mainly a result of coarse spatial and temporal gridding. Elsewhere, minor differences arise since our calculated rivers are smoother than observed ones. The predicted spatial and temporal pattern of cumulative uplift is shown in Figure 5a. These calibrated maps

suggest that African topography grew rapidly over the last 30–40 Ma, in agreement with *Burke* [1996] and *Burke and Gunnell* [2008]. Domal uplift started in North and East Africa. For example, the Hoggar, Tibesti and Afar swells appear early on, which is consistent with their magmatic histories [e.g. *Wilson and Guiraud*, 1992; *Permenter and Oppenheimer*, 2007]. After 30 Ma, the Afar Swell appears to extend southward along the East African Rift. Sub-equatorial topography grew more rapidly during the last 20 Ma, culminating in the appearance of the Bié, Namibian and South African swells. This predicted diachronous growth of topography during Neogene times is largely coeval with the onset of mafic magmatism in North Africa and with increased sedimentary flux into coastal deltas [e.g. *Burke*, 1996; *Walford et al.*, 2005; *Guillocheau et al.*, 2012; *Paul et al.*, 2014]. Figure 6 compares our predicted rates with observed uplift rates based upon emergent marine terraces and uplifted surfaces (Table 1). The inverse algorithm is highly damped which means that rapid, short wavelength, uplift rates along the west and southern Africa tend to be underestimated. Nonetheless, calculated rates are consistent with the long-term pattern of uplift determined from Pliocene marine terraces along the West African margin where a broad axis of uplift decays away from the Bié dome [Figure 5; *Giresse et al.*, 1984; *Guiraud et al.*, 2010]. In southern Africa, stratigraphic evidence suggests that rapid Miocene and Late Pliocene uplift events occurred at rates which are consistent with predicted values [Figure 6; *Partridge & Maud*, 1987, 2000; *Roberts & Brink*, 2002]. In North and East Africa, calculated cumulative uplift rates are consistent with the emergence of Pleistocene-Recent marine terraces with elevations < 100 m [*Hori*, 1970; *Elmejdoub & Jedoui*, 2009].

The spatial and temporal resolution of cumulative uplift is determined by a combination of drainage density and river length. Longer rivers can record older uplift events and in general uplift events within the lower reaches of a drainage network are better resolved than those which occur further upstream. Figure 5b shows the number of drainage loci that constrain the uplift history of each cell within the mesh at different time intervals. Thus African drainage networks appear capable of resolving the principal Cenozoic uplift events.

Finally, different degrees of spatial and temporal smoothing were systematically investigated by running suites of inverse models (Figure 7a–b). These models reveal an expected trade-off between model smoothness and misfit [*Parker*, 1994]. Acceptable models are smooth with small residual misfits. The effect of systematic error on calculated uplift was investigated by inverting a drainage inventory in which elevation along each river prifle was everywhere increased by +100 m. Compared to the original inverse model shown in Figure 5a, recovered uplift rates vary by less than ±0.01 mm/a and cumulative uplift by less than ±200 m at 89% of spatial and temporal nodes (Figure 8).

4.2.2. Australia

The physiography of Australia can be divided into four distinct regions: Eastern Highlands, Western Plateau, Central Lowlands and Coastal Plains [e.g. *Quigley et al.*, 2010]. The Eastern Highlands, which reach elevations of 1–2 km, occupy the length of eastern Australia, which has been a passive margin since Jurassic times. At long wavelengths (> 1000 km) free-air gravity data in eastern Australia is positive (+15–30 mGal; Figure 9a). Admittance studies of the spectral relationship between free-air gravity and topography suggests that the Eastern Highlands are dynamically supported by 0.5–1 km, which

approximately coincides with the elevation of knickzones in eastern Australia [*McKenzie & Fairhead*, 1997; *Czarnota et al.*, 2014; Shoalhaven and Snowy rivers of Figure 10]. Topography of the Western Plateau is more subdued than that of the Eastern Highlands. However, substantial (tens of kilometers long, hundreds of meters high) knickzones occur close to the coastline, which suggests an actively eroding landscape (Figure 10: Swan, Moore, Greenough). The Central Lowlands and Coastal Plains typically have elevations < 100 m.

Offshore, the evolution of dynamic support is constrained by rapid Neogene subsidence of shallow-water carbonate reef deposits [Figure 9d; *Czarnota et al.*, 2014]. Onshore, uplift of southern Australia is recorded by Eocene ($\sim$ 50 Ma), Miocene ($\sim$ 15 Ma) and Pliocene ($\sim$ 5 Ma) marine terraces, which have elevations of $\sim$ 0.5 km, 0.3 km and 0.2 km, respectively [*Sandiford*, 2007]. The existence of Cretaceous coastal and marine strata indicate that most of Australia was at, or below, sea level until $\sim$ 90 Ma. Uplift mainly occurred during the Cenozoic Era [Figure 9c–d; *Langford et al.*, 1995; *Haig & Mory*, 2003]. Cenozoic basaltic and intermediate magmatism peppers the eastern margin [see *Vasconcelos et al.*, 2009 and references therein]. Oligocene and younger igneous rocks in eastern Australia are deeply incised by rivers and record the growth of relief [*Young & McDougall*, 1993]. These data help to calibrate the erosional model. In southeastern Australia, 21 million year old basalt flows have preserved the shapes of ancient river profiles [*Young & McDougall*, 1993].

Since river profiles at two different times are known, best-fitting values of v and m can be identified [e.g. *Stock & Montgomery*, 1999; *Czarnota et al.*, 2014]. In southeastern Australia, $v = 5.96$ m$^{0.4}$/Ma and $m = 0.3$. We have used these values of v and m

to invert an inventory of 253 Australian river profiles as a function of the spatial and temporal uplift rate history. As before, river profiles were extracted from the 3 arc-second SRTM dataset [Figure 9a–b; *Czarnota et al.*, 2014]. These data were compared to satellite imagery, spot-measurements of elevation and published longitudinal profiles [e.g. *van der Beek & Bishop*, 2003; *Brown et al.*, 2011]. Apart from internally drained central regions, the fidelity of the extracted network is high.

Fits between observed and calculated river profiles are shown in Figure 10. The resultant spatial and temporal pattern of cumulative uplift is shown in Figure 11. Figures 11c and 11d show that shorter wavelength uplift can be resolved when a finer spatial grid is employed. However, using a finer resolution uplift grid increases the model's null space (Figure 11d). Our results suggest that the growth of Australian topography took place over the last 70–80 Ma. Eastern Australia has been uplifted by 1–1.5 km since $\sim$ 70 Ma at maximum rates of 0.05–0.1 mm/a (Figure 11a). Western and central Australia have been uplift by 0.5–1 km since $\sim$ 90 Ma. In Figure 12 we compare observed and predicted uplift rates. Predicted rates are consistent with ages of emergent marine terraces in southern Australia [e.g. *Sandiford*, 2007], and with the growth of relief recorded by river incision along the east coast [*Young & McDougall*, 1993; Table 2]. Our calculations are in broad agreement with those of *Czarnota et al.* [2014]. Figure (13a–b) shows the choice of smoothing parameter values used.

5. Conclusions

By building upon the non-linear optimization approach developed by *Pritchard et al.* [2009], *Roberts & White* [2010] and *Roberts et al.* [2012], we have described and applied a linear inverse model that can be used to fit substantial inventories of river profiles and

determine spatial and temporal patterns of uplift rate (see also *Goren et al.*, 2014 and *Fox et al.*, 2014). We show how this scheme is used to calculate uplift rate histories for single or multiple river profiles. The erosional model is a simplified version of the well-known stream-power law that has a linear advective formulation. The governing equation is solved using the method of characteristics. Smooth uplift rate histories, which minimise the misfit between observed and theoretical river profiles are sought using a non-negative least squares approach.

Our results suggest that Africa has largely been uplifted during the last 30 million years. Its domal swells have a diachronous history of uplift, which is consistent with spot measurements of uplift estimated from sub-aerial exposed marine rocks and truncated deltaic stratigraphy on the coastal shelf of West Africa (Figures 3c–d & 5a). The Australian continent also underwent Cenozoic uplift. Eastern Australia was elevated by 1–1.5 km over the last 70 million years. In southwest and southern Australia, our results are consistent with hundreds of meters of post-40 Ma uplift inferred from the elevation of Eocene and younger marine terraces (Figures 9c–d & 10a).

In the examples shown, the erosional parameters, v and m, were calibrated using independently estimated incision or uplift rate histories. v and m trade off negatively with each other and the values we use for Africa are approximately equivalent to $v = 200$ m$^{0.6}$ Ma^{-1} and $m = 0.2$ proposed by *Roberts et al.* [2012]. For Australia, v is a factor of two smaller. It is unclear why v and m vary from continent to continent.

Our results are encouraging since they suggest that drainage networks contain coherent patterns of knickzones that might not be caused by short wavelength (< 10 km) lithologic changes or by temporal discharge variations. Instead, it is conceivable that the evolution

of these networks is controlled by spatial and temporal patterns of regional uplift. We
propose that drainage networks might contain useful, albeit indirect, clues about topo-
graphic evolution and that a global analysis of drainage inventories might be a fruitful
endeavor.

Appendix A: Discretization

Consider the example shown in Figure 15 where uplift rate is permitted to vary as a
function of space and time. Three steps are used to determine an uplift rate history using
the approach outlined in Section 3. First, $dx/dt = -vA^m$ is integrated once. Secondly,
the matrix, M, is constructed. Finally, inversion is carried out using a non-negative linear
least squares approach.

The time taken for a knickzone to travel along a characteristic path is given by Equation
(10) as

$$\tau_{G_j} = \int_{x_n^*}^{x_{n-1}^*} \frac{dx}{vA^m} + \int_{x_{n-1}^*}^{x_{n-2}^*} \dots + \int_{x_{j+1}^*}^{x_j^*} \frac{dx}{vA^m}. \tag{A1}$$

This equation is discretized using the trapezoidal rule where

$$\tau_{G_j} = \sum_{k=j}^{n} \frac{(x_k^* - x_{k+1}^*)}{2} \left(\frac{1}{vA(x_n^*)^m} + \frac{1}{vA(x_{n+1}^*)^m} \right) \tag{A2}$$

where $x_n^* = 0$ at the river mouth and $\tau_{G_n} = 0$ at the present day. In a similar way,
Equation (11) is approximated by

$$\tau_{G_j} - T_{ij} = \int_0^{x_i^*} \frac{dx}{vA^m} = \tau_{G_i} \tag{A3}$$

so that

$$T_{ij} = \tau_{G_j} - \tau_{G_i}, \qquad i = j, j+1, \dots n. \tag{A4}$$

T_{ij} are values of time along the characteristic curve that is located at $x = 0$ and $t = \tau_{G_j}$
where distances and elevations along the river are known (i.e. $x(T_{ij}) = x_i$).

Uplift rate, U, is defined at discrete times (e.g. $t_1, t_2, \ldots, t_6$) and at discrete positions. At intermediate times and positions, U is obtained by linear interpolation. Elevations are determined by integrating uplift rates along characteristic paths using the trapezoidal rule. Uplift rate histories are integrated between nodes whose loci are defined by t and x (e.g. black dots in Figure 15). Equation (12) is given by

$$z_j = \int_{S_{1_j}}^{S_{2_j}} U(\mathbf{x}(t), t) \, \mathrm{d}t + \int_{S_{2_j}}^{S_{3_j}} \ldots \tag{A5}$$

where $\mathbf{x}(t)$ is the position in space along the characteristic curve at time t. This equation is approximated by

$$z_j^* = \sum_{k=1}^{m(j)} \frac{(S_{k+1,j} - S_{k_j})}{2} \left[U(\mathbf{x}(S_{k+1,j}), S_{k+1,j}) + U(\mathbf{x}(S_{k,j}), S_{k,j}) \right] \tag{A6}$$

where S_{ij} consists of dividing the integral up, both by times T_{ij}, at which the position of the river is known, and by times $t_1, t_2, \ldots$ at which uplift times are discretized. $m(j)$ is the number of points on characteristic curve j (i.e. 12 points on τ_{G_1}). At time T_{ij}, linear interpolation in time is carried out so that

$$U(T_{ij}, \mathbf{x}(T_{ij})) = U(T_{ij}, \mathbf{x}_i) = \frac{[T_{ij}^+ - T_{ij}] U(T_{ij}^+, \mathbf{x}_i) + [T_{ij} - T_{ij}^-] U(T_{ij}^-, \mathbf{x}_i)}{T_{ij}^+ - T_{ij}^-} \tag{A7}$$

T_{ij}^+ and T_{ij}^- are time nodes which bracket T_{ij}. At a time t_i, a linear interpolation in space is carried out so that

$$U(t_i, \mathbf{x}(t_i)) = \alpha U(t_i, \mathbf{x}_a) + \beta U(t_i, \mathbf{x}_b) + \gamma U(t_i, \mathbf{x}_c) \tag{A8}$$

where α, β and γ are the barycentric weights for position $\mathbf{x}(t_i)$ (Figure 14). $\mathbf{x}_a$, $\mathbf{x}_b$ and $\mathbf{x}_c$ are the mesh nodes of the triangle containing $\mathbf{x}(t_i)$.

There is now a linear relationship between each river elevation, z_j^*, and uplift rate at each space and time node which can be cast in matrix form as

$$\mathbf{z} = M\mathbf{U}. \qquad (A9)$$

References

Al-Hajri, Y., White, N. & Fishwick, S. (2009), Scales of transient convective support beneath Africa, *GSA Bulletin, 37*(10), 883–886.

Anderson, R. S. and Anderson, S. P. (2010), Geomorphology: The Mechanics and Chemistry of Landscapes, *Cambridge University Press*, 651 p.

van der Beek, P. and P. Bishop (2003), Cenozoic river profile development in the Upper Lachlan catchment (SE Australia) as a test of quantitative fluvial incision models, *J. Geophys. Res., 108*(B6), doi:10.1029/2002jb002125.

Brown, N. J., W. E. Featherstone, G. Hu, and G. M. Johnston (2011), AUSGeoid09: a more direct and more accurate model for converting ellipsoidal heights to AHD heights, *J. Spat. Sci.*, *56*(1), 27–37.

Broyden, C. G., J. E. Dennis Jr. and J. Moré (1973) On the Local and Superlinear Convergence of Quasi-Newton Methods, *J. Inst. Maths Applics*, *12*, 223–245.

Burke, K. (1996), The African plate, *S. Afr. J. Geol.*, *99*(4), 341–409.

Burke, K., and Gunnell, Y. (2008), A Continental-Scale Synthesis of Geomorphology, Tectonics, and Environmental Change over the Past 180 Million Years, *GSA Memoir*, *201*.

Berlin, M. M., and Anderson, R. S. (2007), Modeling of knickpoint retreat on the Roan Plateau, western Colorado, *J. Geophys. Res.*, *112*(F03S06), doi:10.1029/2006JF000553.

Croissant, T. & Braun, J. (2014), Constraining the stream power law: a novel approach combining a landscape evolution model and an inversion method, *Earth Surf. Dynam.*, *2*, 155–166.

Crosby, A. C., McKenzie, D. & Sclater, J. G. (2006), The relationship between depth, age and gravity in the oceans, *Geophys. J. Int.*, *166*, 553–573.

Czarnota, K. C., Roberts, G. G., White, N. J. & Fishwick, S. (2014), Spatial and Temporal Pattern of Australian Dynamic Topography from River Profile Modeling, *J. Geophys. Res: Solid Earth*, *119*, doi:10.1002/2013JB010436.

Elmejdoub, N. & Jedoui, Y. (2009), Pleistocene raised marine deposits of the Cap Bon peninsula (N–E Tunisia): Records of sea-level highstands, climatic changes and coastal uplift, *Geomorphology, 112*, 179–189.

Erlanger, E. D., Granger, D. E. & Gibbon, R. J. (2012), Rock uplift rates in South Africa from isochron burial dating of fluvial and marine terraces, *Geology, 40*(11), 1019–1022.

Farr, T. G., P. A. Rosen, E. Caro, R. Crippen, R. Duren, S. Hensley, M. Kobrick, M. Paller, E. Rodriguez, L. Roth, D. Seal, S. Shaffer, J. Shimada, J. Umland, M. Werner, M. Oskin, D. Burbank, and D. Alsdorf (2007), The Shuttle Radar Topographic Mission, *Reviews of Geophysics, 45*, doi:1029/2005RG000,183.

Flament, N., Gurnis, M. & Muller, R. D. (2013), A review of observations and models of dynamic topography, *Lithosphere, 5*(2), 189–210.

Flowers, R. M., Wernicke, B. P., & Farley, K. A. (2008), Unroofing, incision, and uplift history of the southwestern Colorado Plateau from apatite (U-Th)/He thermochronometry, *GSA Bulletin, 1*20(5/6), 571–587.

Fox, M., Goren, L., May, D. A. & Willett, S. D. (2014), Inversion of fluvial channels for paleorock uplift rate in Taiwan, *J. Geophys. Res. Earth Surface, 1*19, 1853–1875, doi:10.1002/2014JF003196.

Galloway, W. E., Whiteaker, T. L. & Ganey-Curry, P. (2011), History of Cenozoic North American drainage basin evolution, sediment yield, and accumulation in the Gulf of Mexico basin, *Geosphere, 7*(4), 938–973.

Ghosh, P., Garzione, C. N. & Eiler, J. M. (2006), Rapid Uplift of the Altiplano Revealed Through ^{13}C-^{18}O Bonds in Paleosol Carbonates, *Science, 3*11(5760), 511–515.

Giresse, P., Hoang, C.-T. & Kouyoumontzakis, G. (1984), Analysis of vertical movements deduced from a geochronological study of marine Pleistocene deposits, southern coast of Angola, *J. Afr. Earth Sci., 2*(2), 177–187.

Giresse, P., Barusseau, J.-P., Causse, C. & Diouf, B. (2000), Successions of sea-level changes during the Pleistocene in Mauritania and Senegal distinguished by sedimentary facies study and U/Th dating, *Mar. Geol., 1*70, 123–139.

Goren, L., Fox, M. & Willett, S. D. (2014), Tectonics from fluvial topography using formal linear inversion: Theory and applications to the Inyo Mountains, California, *J. Geophys. Res. Earth Surface*, *119*, doi:10.1002/2014JF003079.

Guiraud, M., Buta-Neto, A. & Quesne, D. (2010), Segmentation and differential post-rift uplift at the Angola margin as recorded by the transform-rifted Benguela and oblique-to-orthogonal-rifted Kwanza basins, *Marine and Petroleum Geology,* 1040–1068.

Guillocheau, F., Rouby, D., Robin, C., Helm, C., Rolland, N., Le Carlier de Veslud, C. & Braun, J. (2012), Quantification and causes of the terrigeneous sediment budget at the scale of a continental margin: a new method applied to the Namibia—South Africa margin, *Basin Res., 24*, 3–30.

Gurnis, M., Mitrovica, J. X., Ritsema, J. & van Heijst, H.-J. (2000), Constraining mantle density structure using geological evidence of surface uplift rates: The case of the African Superplume, *Geochem. Geophys. Geosys.,* 1, doi:10.1029/1999GC000035.

Hack, J. T. (1957), Studies of longitudinal stream profiles in Virginia and Maryland, *U.S. Geological Survey Professional Paper, 294-B*, 45–97.

Haig, D. W. & Mory, A. J. (2003), New record of siliceous, marine, later Eocene from Kalbarri, Western Australia, *J. Royal Soc. West. Aust. 86*, 107–113.

Holmes, A. (1944), Principles of Physical Geology, *Edinburgh, Thomas Nelson and Sons Limited*, 532 p.

Hori, N. (1970), Raised Coral Reefs along the Southeastern Coast of Kenya, East Africa, *Geog. Rep. Tokyo Met. Uni.*, *5*, 25–47.

Howard, A., M. Seidl, and W. Dietrich (1994), Modeling fluvial erosion on regional to continental scales, *J. Geophys. Res.*, *99*, 13,971–13,986.

Howard, A. D. & Kerby, G. (1983), Channel changes in badlands, *GSA Bulletin 94*, 739–752.

Jackson, M. P. A., M. R. Hudec, and K. A. Hegarty (2005), The great West African Tertiary coastal uplift: Fact or Fiction? A perspective from the Angolan divergent margin, *Tectonics*, *24*, TC6014, doi:10.1029/2005TC001863.

Jedoui, Y., Reyss, J. L., Kallel, N., Montacer, M., Ben Ismail, H. and Davaud, E. (2003), U-series evidence for two high Last Interglacial sea-levels in southeastern Tunisia, *Quat. Sci. Rev., 22*, 343–351.

Jones, S. M., Lovell, B. & Crosby, A. G. (2012), Comparison of modern and geological observations of dynamic support from mantle convection, *J. Geol. Soc. London, 169*, 745–758.

King, L. (1962), *The Morphology of the Earth: A study and synthesis of world scenery*, London, Oliver and Boyd.

Kuhn, H. W. and Tucker, A. W. (1951), *Nonlinear Programming*, Proc. Second Berkeley Symp. on Math. Statist. and Prob., Univ. of Calif. Press, 481–492

Lague, D. (2014), The stream power river incision model: evidence, theory and beyond, *Earth Surf. Process. Landforms 39*, 38–61.

Langford, R., G. Wilford, E. Truswell, & A. Isern (1995), Palaeogeographic atlas of Australia—Cainozoic, Cretaceous, *Australian Geological Survey Organisation, Canberra*

574   *10.*

575   Lawson, C. L. & Hanson, R. J. (1987), Solving Least Squares Problems *Prentice-Hall.*

576   Leturmy, P., F. Lucazeau, and F. Brigaud (2003), Dynamic interactions between the gulf

577   of Guinea passive margin and the Congo River drainage basin: 1 Morphology and mass

578   balance, *J. Geophys. Res.*, *108* (B8), doi:10.1029/2002JB001927.

579   Lighthill, M. J. & Whitham, G. B. (1955), On kinematic waves, *Proc. Roy. Soc. London*,

580   Series A, Mathematical and Physical Sciences, *229* (1178), 281–316.

581   Logg, A., K.-A. Mardal, & G. N. Wells (2012), Automated Solution of Differential Equa-

582   tions by the Finite Element Method, *Springer*, doi:10.1007/978-3-642-23099-8.

583   Lucazeau, F., F. Brigaud, and P. Leturmy (2003), Dynamic interactions between the gulf

584   of Guinea passive margin and the Congo River drainage basin: 2 Isostasy and uplift, *J.*

585   *Geophys. Res.*, *108* (B8), doi:10.1029/2002JB001928.

586   Luke, J. C. (1972), Mathematical Models for Landform Evolution, *J. Geophys. Res.*

587   *77* (14), 623–649.

588   McKenzie, D. & Fairhead, D. (1997), Estimates of the effective elastic thickness of the

589   continental lithosphere from bouguer and free-air gravity anomalies, *J. Geophys. Res.*

590   *102* (B12), 2460–2464.

591   Meghraoui, M., Outtani, R., Choukri, A. & Frizon De Lamotte, D. (1998), Coastal tec-

592   tonics across the South Atlas thrust front and the Agadir active zone, Morocco, in:

593   Stewart, I. S. & Vita-Finzi, C. (eds) *Coastal Tectonics,* Geol. Soc., London, Spec. Pub.

594   *146*, 239–253.

595   Miller, K., Kominz, M. A., Browning, J. V., Wright, J. D., Mountain, G. S.,

596   Katz, M. E., Sugarman, P. J., Cramer, B. S., Christie-Blick, N. & Pekar, S. F.

(2005), The Phanerozoic Record of Global Sea-Level Change, *Science, 310*(1293), doi:10.1126/science.1116412.

Mudd, S. M., Attal, M., Milodowski, D. T., Grieve, S. W. D. & Valters, D. A. (2014), A statistical framework to quantify spatial variation in channel gradients using the integral method of channel profile analysis, *J. Geophys. Res. Earth Surf., 119*(2), doi:10.1002/2013JF002981.

Moucha, R. & Forte, A. M. (2011), Changes in African topography driven by mantle convection, *Nat. Geo. 4*, doi:10.1038/ngeo1235.

Nyblade, A. A., and S. W. Robinson (1994), The African Superswell, *Geophys. Res. Lett., 21*, 765–768.

Odada, E. O. (1996), Geological evolution of coastal Kenya as inferred from sedimentary sequences and marine terraces, *Afr. Geosci. Rev., 3*(3), 1–18.

Parker, R. L. (1994), Geophysical Inverse Theory, *Princeton University Press.*

Partridge, T. C. (1997), Cainozoic environmental change in southern Africa, with special emphasis on the last 200,000 years, *Proc. Phys. Geog. 21*(1), 3–22.

Partridge, T. C. (1998), Of diamonds, dinosaurs and diastophism; 150 million years of landscape evolution in southern Africa, *S. Afr. J. Geol. 101*(3), 167–184.

Partridge, T. C. & Maud, R. R. (1987), Geomorphic evolution of Southern Africa since the Mesozoic, *S. Afr. J. Geol. 90*(2), 179–208.

Partridge, T. C. & Maud, R. R. (2000), Macro-scale geomorphic evolution of southern Africa. In: Partridge, T. C. & Maud, R. R. (Eds.), The Cenozoic of Southern Africa. Oxford University Press, New York, 3–18.

Paul, J. D, Roberts, G. G., & White, N. J. (2014), The African Landscape Through Space and Time, *Tectonics 32*, doi:10.1002/2013TC003479.

Pedoja, K., Husson, L., Regard, V., Cobbold, P. R., Ostanciaux, E., Johnson, M. E., Kershaw, S., Saillard, M., Martinod, J., Furgerot, L., Weill, P., Delcaillau, D. (2011), Relative sea-level fall since the last interglacial stage: Are coasts uplifting worldwide?, *Earth-Science Reviews 108*, 1–15.

Permenter, J. L., and C. Oppenheimer (2007), Volcanoes of the Tibesti massif (Chad, northern Africa), *Bull. Volcanol.*, *69*, 609–626.

Pritchard, D., Roberts, G. G., White, N. J. & Richardson, C. N. (2009), Uplift histories from river profiles, *Geophys. Res. Lett., 36*(L24301), doi:10.1029/2009GL040928.

Quigley, M. C., Clark, D., & Sandiford, M. (2010), Tectonic geomorphology of Australia, *Geol. Soc. London. Spec. Pub., 346*, 243-265.

Raymond, O., Liu, S., Gallagher, R., Highet, L. M., Zhang, W. (2012), Surface geology of Australia 1:2,500,000 scale, 2012 ed., [Digital Dataset], Geoscience Australia, Commonwealth of Australia, Canberra, Australia.

Roberts, D. L. & Brink, J. S. (2002), Dating and correlation of Neogene coastal deposits in the Western Cape (South Africa): Implications for Neotectonism, *S. Afr. J. Geol. 105*, 337–352.

Roberts, G. G. & White, N. J. (2010), Estimating uplift rate histories from river profiles using African examples, *J. Geophys. Res. 115*(B02406), doi:10.0129/2009JB006692.

Roberts, G. G., Paul, J. D., White, N. & Winterbourne, J. (2012), Temporal and spatial evolution of dynamic support from river profiles: A framework for Madagascar, *Geochem. Geophys. Geosys. 13*(1), doi:10.0129/2012GC004040.

Rosenbloom, N. A. & Anderson, R. S. (1994), Hillslope and channel evolution in a marine landscape, Santa Cruz, California, *J. Geophys. Res. 99*(B7), 14,013–14,029.

Royden, L. & Perron, J. T. (2013), Solutions of the stream power equation and application to the evolution of river longitudinal profiles, *J. Geophys. Res.: Earth Surf. 118*, doi:10.1002/jgrf.20031.

Sahagian, D. (1988), Epeirogenic motions of Africa as inferred from Cretaceous shoreline deposits, *Tectonics, 7*(1), 125–138.

Sandiford, M. (2007), The tilting continent: A new constraint on the dynamic topographic field from Australia, *Earth and Planetary Science Letters, 261*, 152–163.

Sklar, L. S. & Dietrich, W. E. (1998), River longitudinal profiles and bedrock incision models: Stream power and influence of sediment supply, *Rivers Over Rock: Fluvial Processes in Bedrock Channels. Geophys. Mono., 107*, 237–260.

Sklar, L. S. & Dietrich, W. E. (2001), Sediment and rock strength control on river incision into bedrock, *Geology, 29*(12), 1087–1090.

Smith, T. R., Merchant, G. E. & Birnir, B. (2000), Transient attractors: towards a theory of the graded stream for alluvial and bedrock channels, *Computers & Geoscience, 26*, 541–580.

Smith, W. H. F. & Wessel, P. (1990), Gridding with continuous curvature splines in tension, *Geophysics, 55*(3), 293–305.

Stock, J. D. & Montgomery, D. R. (1999), Geologic constraints on bedrock river incision using the stream power law, *J. Geophys. Res., 104*(B3), 4983–4993.

Strahler, A. N. (1957), Quantitative Analysis of Watershed Geomorphology, *Trans. Am. Geophys. Union, 38*(6), 913–920.

Tanaka, K., Hataya, R., Spooner, N. A., Questiaux, D. G., Saito, Y. & Hashimoto, T. (1997), Dating of marine terrace sediments by ESR, TL and OSL methods and their applicabilities, *Quaternary Science Reviews, 16*(3–5), 257–264.

Tapley, B., J. Ries, S. Bettadpur, D. Chambers, M. Cheng, F. Condi, B. Gunter, Z. Kang, P. Nagel, R. Paster, T. Pekker, S. Poole, and F. Wang (2005), GGM02 — An improved Earth gravity field model from GRACE, *Journal of Geodesy, 79*(8), 467–478.

Tomkin, J. H., Brandon, M. T., Pazzaglia, F. J., Barbour, J. R. & Willett, S. D. (2003), Quantitative testing of bedrock incision models for the Clearwater River, NW Washington State , *J. Geophys. Res., 108*(B6), 2308, doi:10.1029/2001JB000862.

Van der Wateren, F. M. & Dunai, T. J. (2001), Late Neogene passive margin denudation history—cosmogenic isotope measurements from the central Namib desert , *Global and Planetary Change,30*, 271–307.

Vasconcelos, P. M., Knesel, K. M., Cohen, B. E. & Heim, J. A. (2009), Geochronology of the Australian Cenozoic: a history of tectonic and igneous activity, weathering, erosion, and sedimentation, *Aust. J. Earth Sci., 55*, 865–914.

Wellman, P. (1987), Eastern Highlands of Australia; their uplift and erosion, *BMR J. Aust. Geol. Geophys., 4*, 373–382.

Walford, H. L., White, N. J. & Sydow, J. C. (2005), Solid sediment load history of the Zambezi Delta, *Earth and Planetary Science Letters, 238*, 49–63.

Weissel, J. K. & Seidl, M. A. (1998), Inland propagation of erosional escarpments and river profile evolution across the southeastern Australian passive continental margin, *in: Rivers Over Rock, Geophys. Mono., 107*, 189–206.

Whipple, K. X. & Tucker, G. E. (1999), Dynamics of the stream-power river incision model: Implications for height limits of mountain ranges, landscape response timescales, and research needs, *J. Geophys. Res., 104* (B8), 17,661–17,674.

Whipple, K. X. & Tucker, G. E. (2002), Implications of sediment-flux-dependent river incision models for landscape evolution, *J. Geophys. Res., 107* (B2), doi:10.1029/2000JB000044.

Wilson, M., and R. Guiraud (1992), Magmatism and rifting in Western and Central Africa, from Late Jurassic to Recent times, *Tectonophysics, 213*, 203–225.

Willett, S. D., McCoy, S. W., Perron, T. J., Goren, L. and Chen, C.-Y. (2014), Dynamic Reorganization of River Basins, *Science, 343*, doi:10.1126/science.1248765.

Winterbourne, J., White, N. & Crosby, A. (2014), Accurate Measurements of Residual Topography in the Oceanic Realm, *Tectonics*, doi:10.1002/2013TC003372.

Whittaker, A. C., Cowie, P. A., Attal, M., Tucker, G. E. and Roberts, G. P. (2007), Contrasting transient and steady-state rivers crossing active normal faults: new field observations from the Central Apennines, Italy, *Basin Research, 9*, 529–556.

Whittaker, A. C. and Boulton, S. J. (2012), Tectonic and climatic controls on knickpoint retreat rates and landscape response times, *J. Geophys. Res., 117*, doi:10.1029/2011JF002157.

Young, R. & McDougall, I. (1993), Long-Term Landscape Evolution: Early Miocene and Modern Rivers in Southern New South Wales, Australia, *J. Geol., 101*, 35–49.
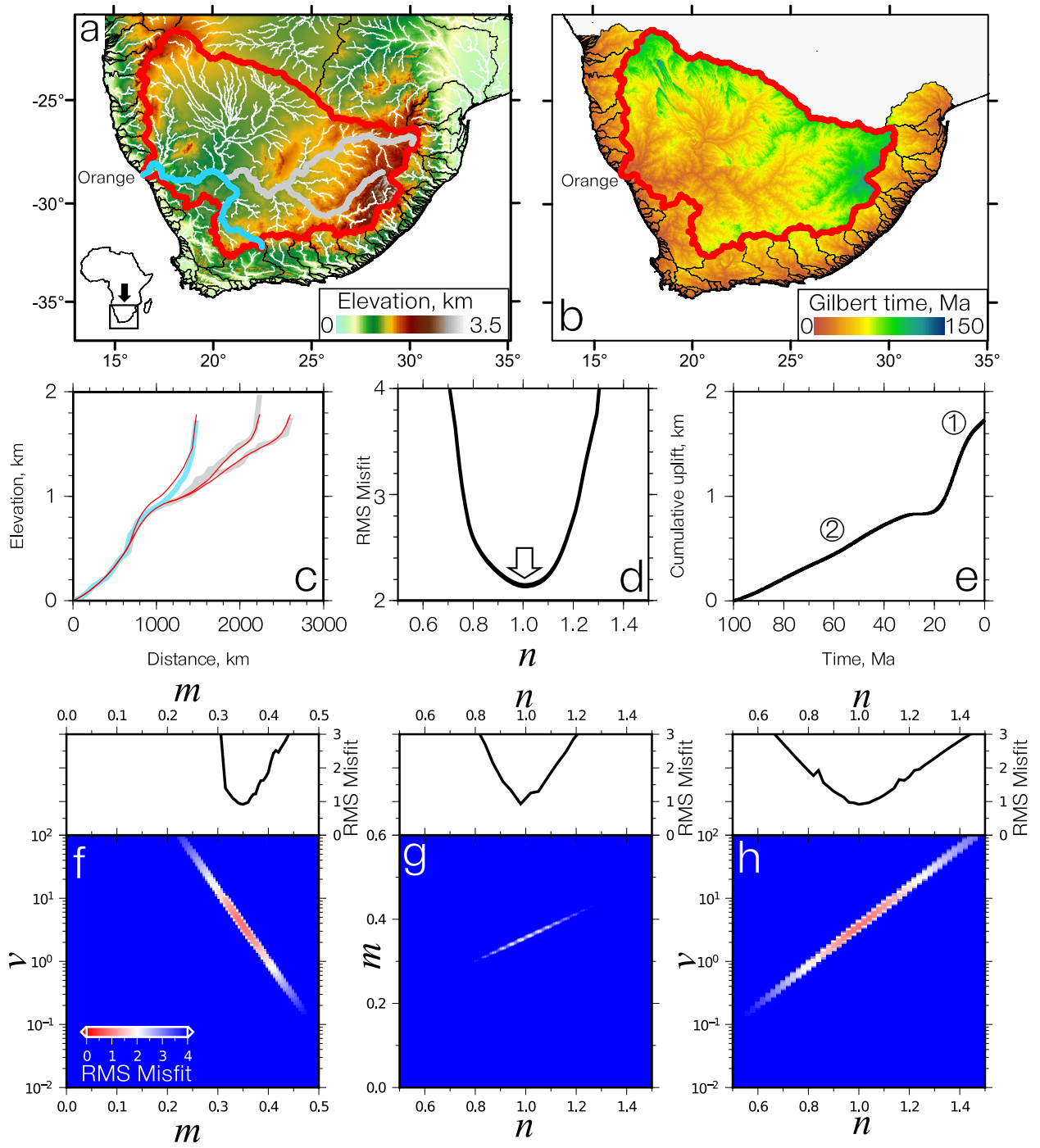
Figure 1. Inverse modeling of Orange river and its tributaries. (a) Topography and drainage of southern Africa. White lines = drainage network; black lines = drainage divides; red line = Orange catchment; gray/blue lines = modeled tributaries. (b) Landscape response time, τ_G, for map shown in (a). (c) Joint inversion of three tributaries of Orange river for $U(t)$. Gray/blue lines = observed profiles; red lines = predicted profiles for $n = 1$. (d) Residual rms misfit between observed and calculated river profiles as function of n from joint-inversion. Arrow indicates global minimum at $n = 1$. (e) Cumulative uplift as function of time determined by general, non-linear, optimization algorithm for single tributary of Orange river with $n = 1$ (blue lines in panels a and c). Encircled numbers = principal uplift events (cf. linearized inversion; Figure 2c). (f) Main panel shows rms misfit between observed and calculated Orange tributary (blue line, panel c) when v and m are co-varied in series of forward models with fixed uplift rate history. Input uplift history shown in panel (e). Upper panel shows misfit variation along trade-off relationship. (g) Main panel shows rms misfit when m and n are co-varied for fixed uplift rate history shown in (e). Upper panel shows misfit variation along trade-off relationship. (h) Main panel shows rms misfit when v and n are co-varied for fixed uplift rate history shown in (e). Upper panel shows misfit variation along trade-off relationship.
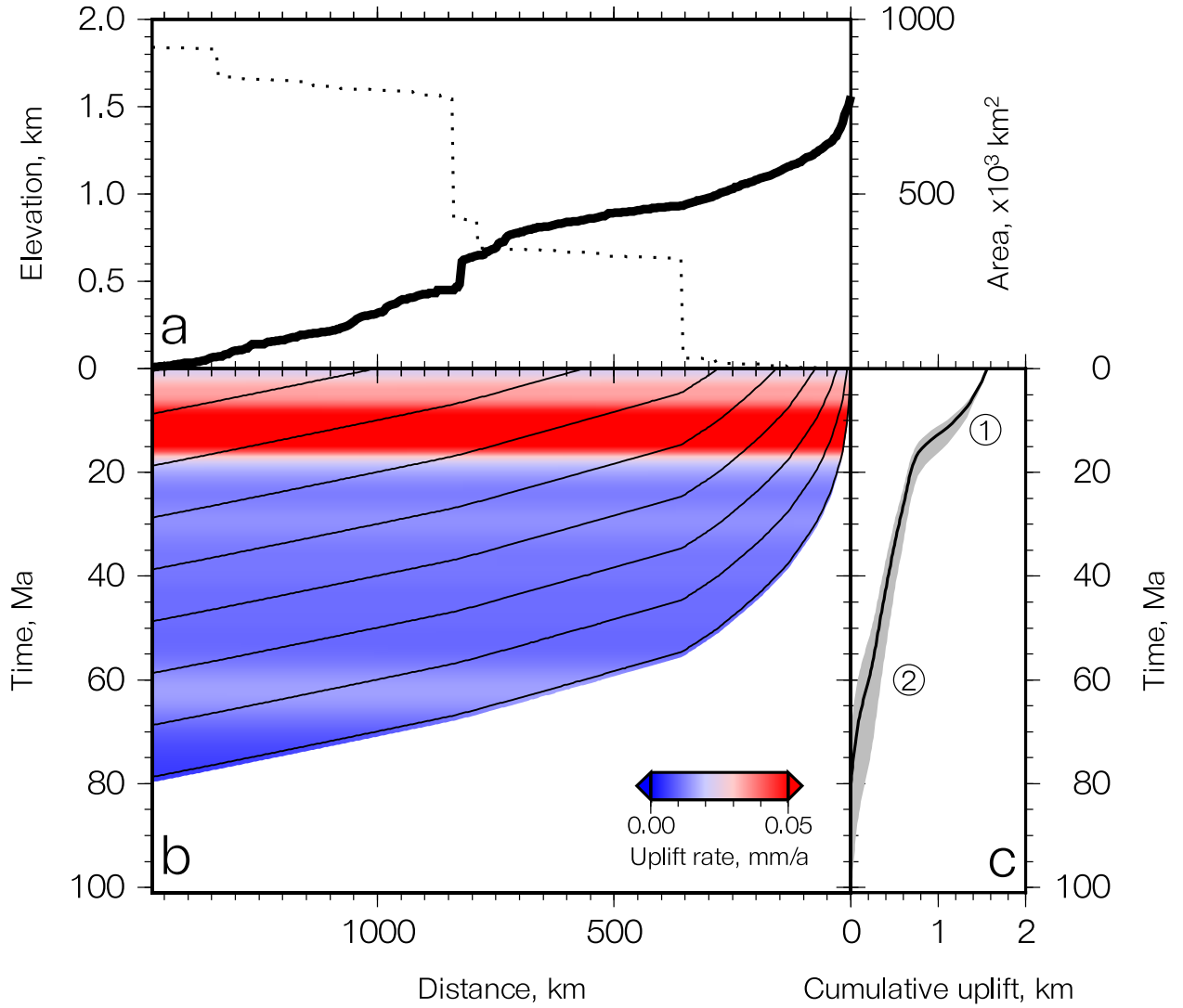
Figure 2. Linear inverse model of Orange river. (a) Solid line = observed river profile (i.e. blue line in Figure 1a); dotted line = observed upstream drainage area, A. (b) Solid lines = characteristic paths of river profile plotted for $vA^m = 3.62A^{0.35}$; colored bands = uplift rate history determined by linearized inverse model. (c) Solid line = cumulative uplift history obtained by integrating over uplift rate history; gray band = range of uncertainty for $A \pm 0.5A$; encircled numbers = principal uplift events (cf. Figure 1e).
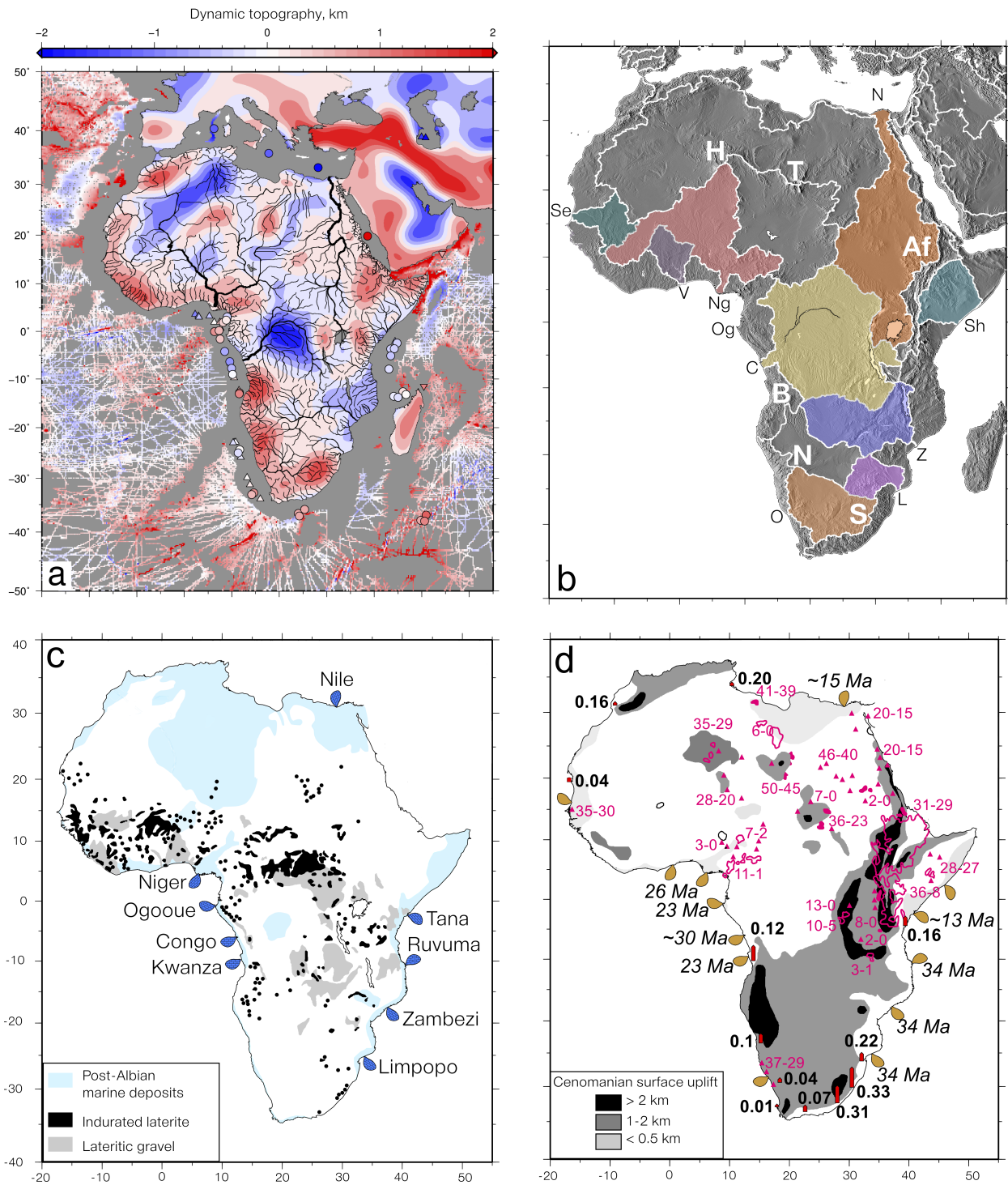
Figure 3.   Independent geologic constraints for Africa. (a) Present-day dynamic support and drainage. Onshore red and blue pattern = positive and negative long wavelength free-air gravity anomalies filtered to remove wavelengths < 800 km, with 10 mgal interval; offshore circles/triangles/filigree = residual bathymetric measurements [*Winterbourne et al.*, 2014]. Black drainage network = 704 rivers extracted from SRTM dataset. (b) Major drainage basins. Se = Senegal, V = Volta, Ng = Niger, Og = Ogooue, C = Congo, O = Orange, L = Limpopo, Z = Zambezi, Sh = Shebelle, N = Nile. Domal swells: H = Hoggar, T = Tibesti, B = Bié, N = Namibia, S = South Africa, Af = Afar. (c) Pre-Oligocene paleogeography of Africa. Blue lobes = deltas with Paleogene reef deposits; light-blue shading = Cretaceous marine sedimentary rocks; gray/black circles = distribution of Cretaceous-Neogene laterites [*Sahagian*, 1988; *Burke*, 1996; *Burke and Gunnell*, 2008; *Paul et al.*, 2014]. (d) Neogene paleogeography; pink polygons = basaltic magmatism; yellow polygons = clastic deltaic deposition; numbered red arrows = observed Neogene-Recent uplift rates where height is proportional to rate in mm/a [*Burke*, 1996; *Paul et al.*, 2014].
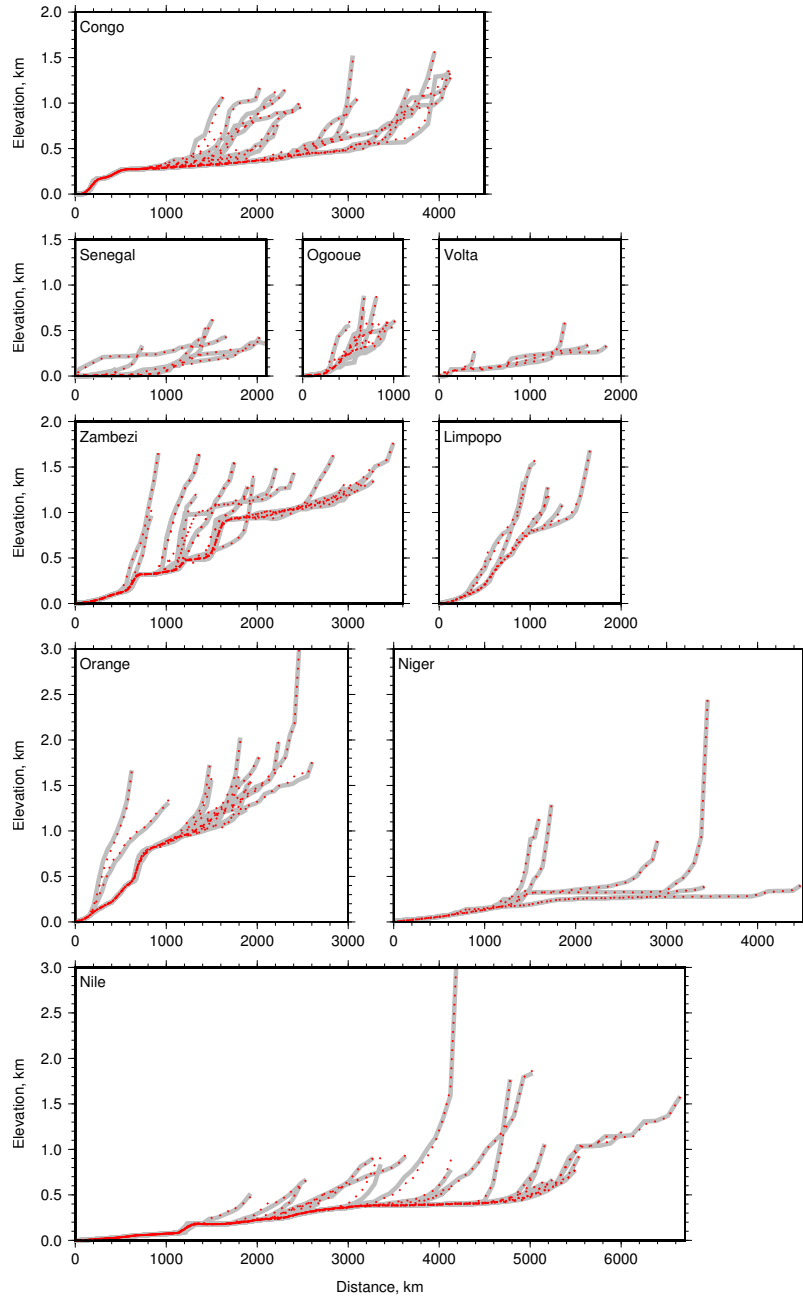
Figure 4. Inverse modeling of African river profiles arranged by catchment, which yields spatial and temporal pattern of cumulative uplift shown in Figure 5. Gray lines = observed river profiles; red dotted lines = best-fit theoretical river profiles generated using uplift history shown in Figure 5. Residual rms misfit = 2.4.
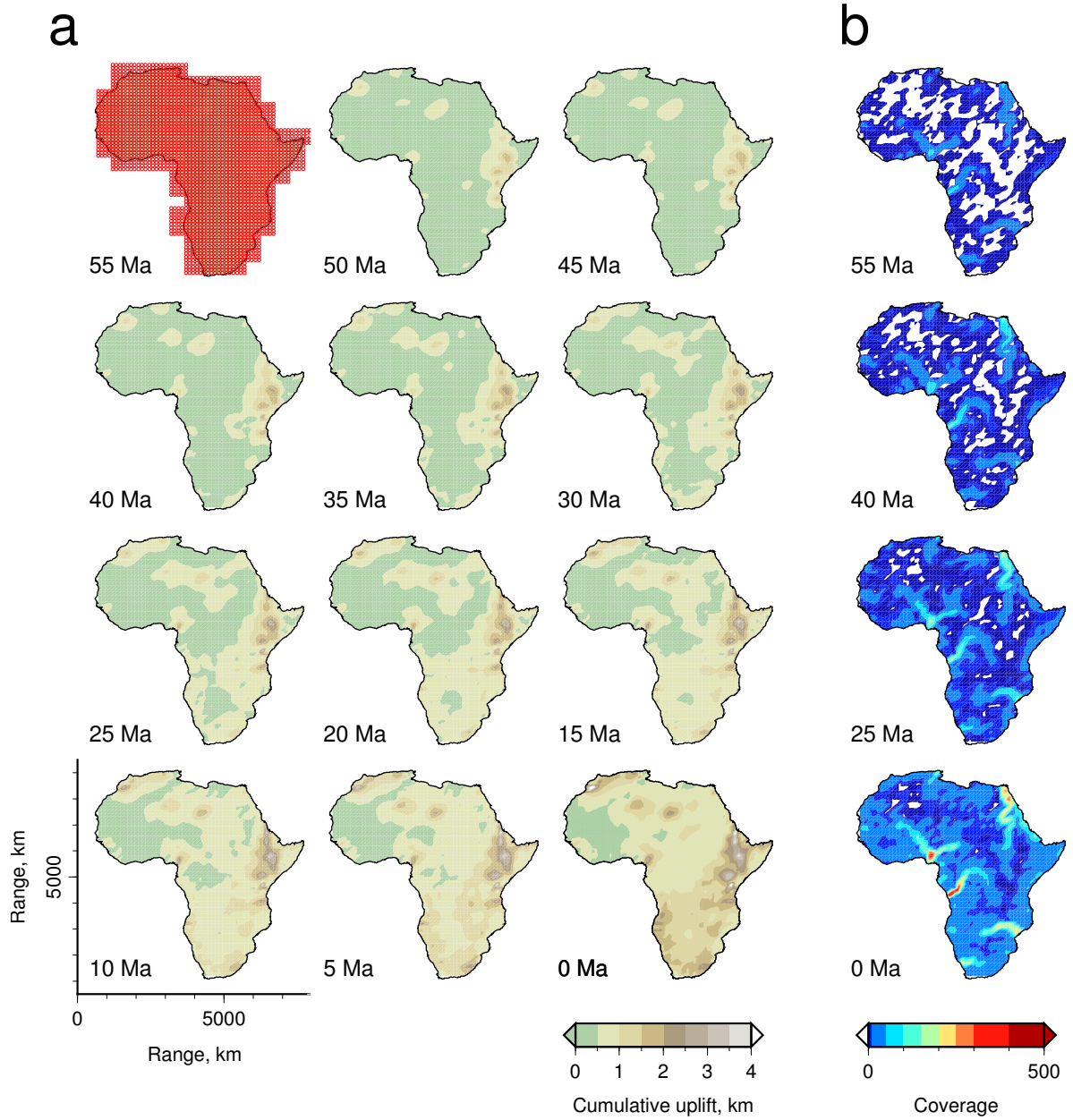
Figure 5. (a) Spatial and temporal pattern of cumulative uplift history for Africa from 55 Ma to present day at 5 Ma intervals. Red circles overlying left-hand panel = spatial regularization grid where triangular mesh = ☑. (b) Selected panels at four different times, which show number of non-zero entries in model matrix, M, corresponding to a given uplift node.
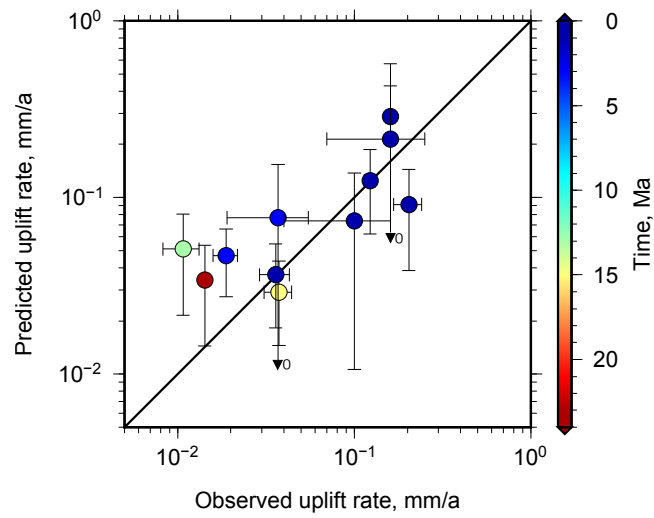
Figure 6.   Comparison of observed and calculated uplift rates for Africa. Circles = weighted mean values of uplift rate where color indicates age (Table 1); vertical/horizontal lines with bars/arrows = uncertainties.
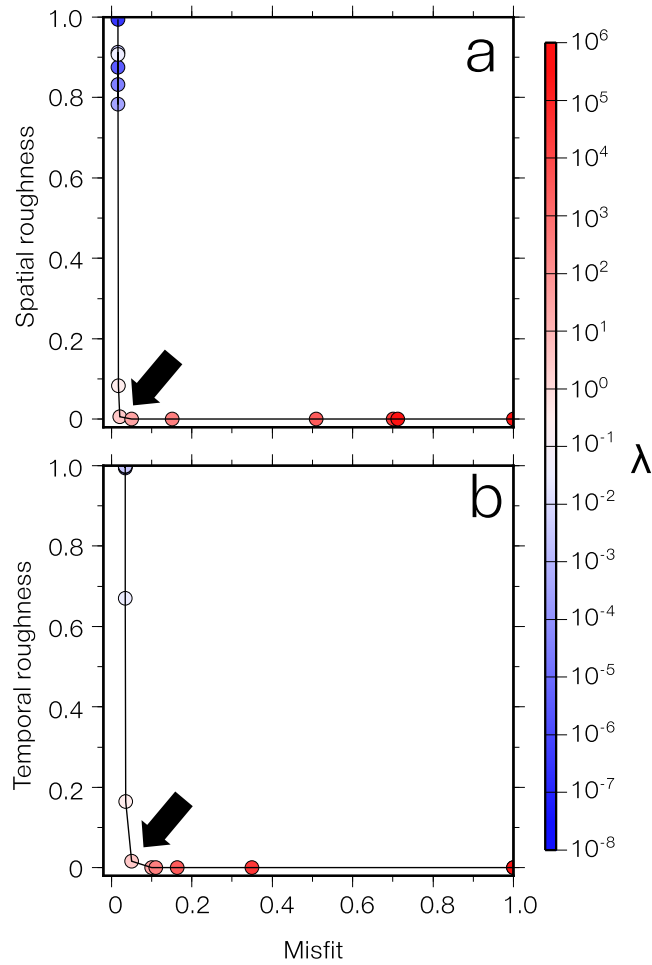
Figure 7. Model regularisation. (a) Misfit, normalized by maximum misfit, as function of spatial smoothing for series of inverse models of 704 river profiles from Africa. Colored circles = individual inverse models for different values of λ_S; black arrow = optimal inverse model. (b) Normalised misfit as function of temporal smoothing. Colored circles = individual inverse models for different values of λ_T.

Figure 8.   Systematic error analysis for Africa. (a) Difference between calculated uplift rates at all spatial and temporal nodes for original and modified (i.e. all elevations increased by 100 m) drainage inventories. (b) Difference between calculated cumulative uplift for original and modified drainage inventories.

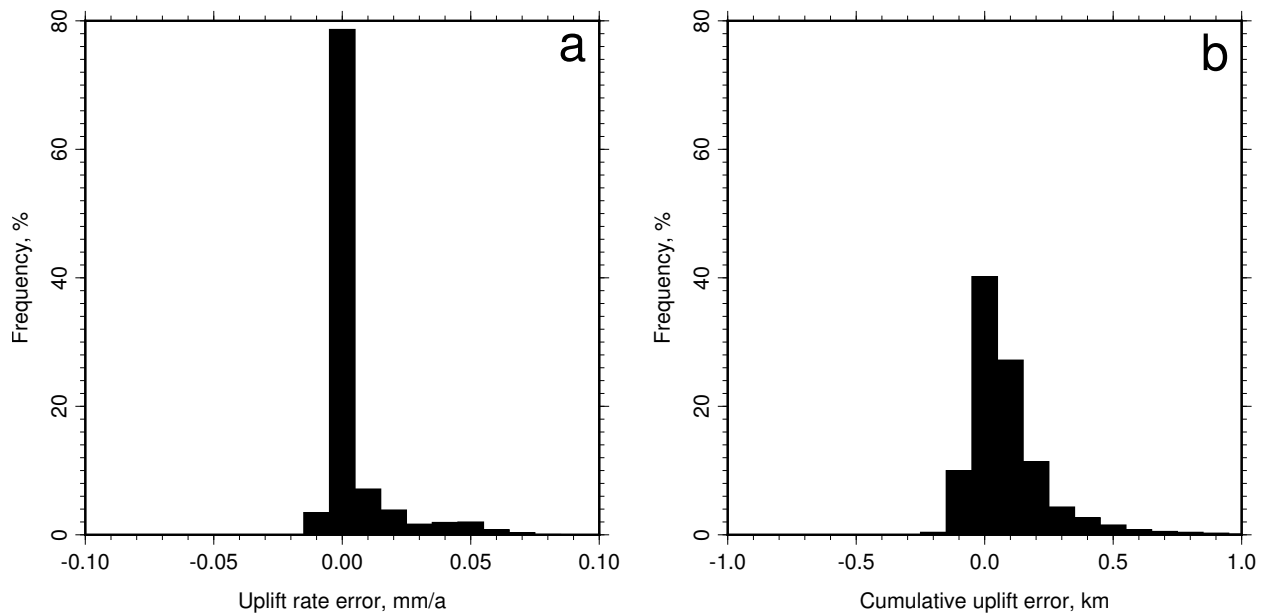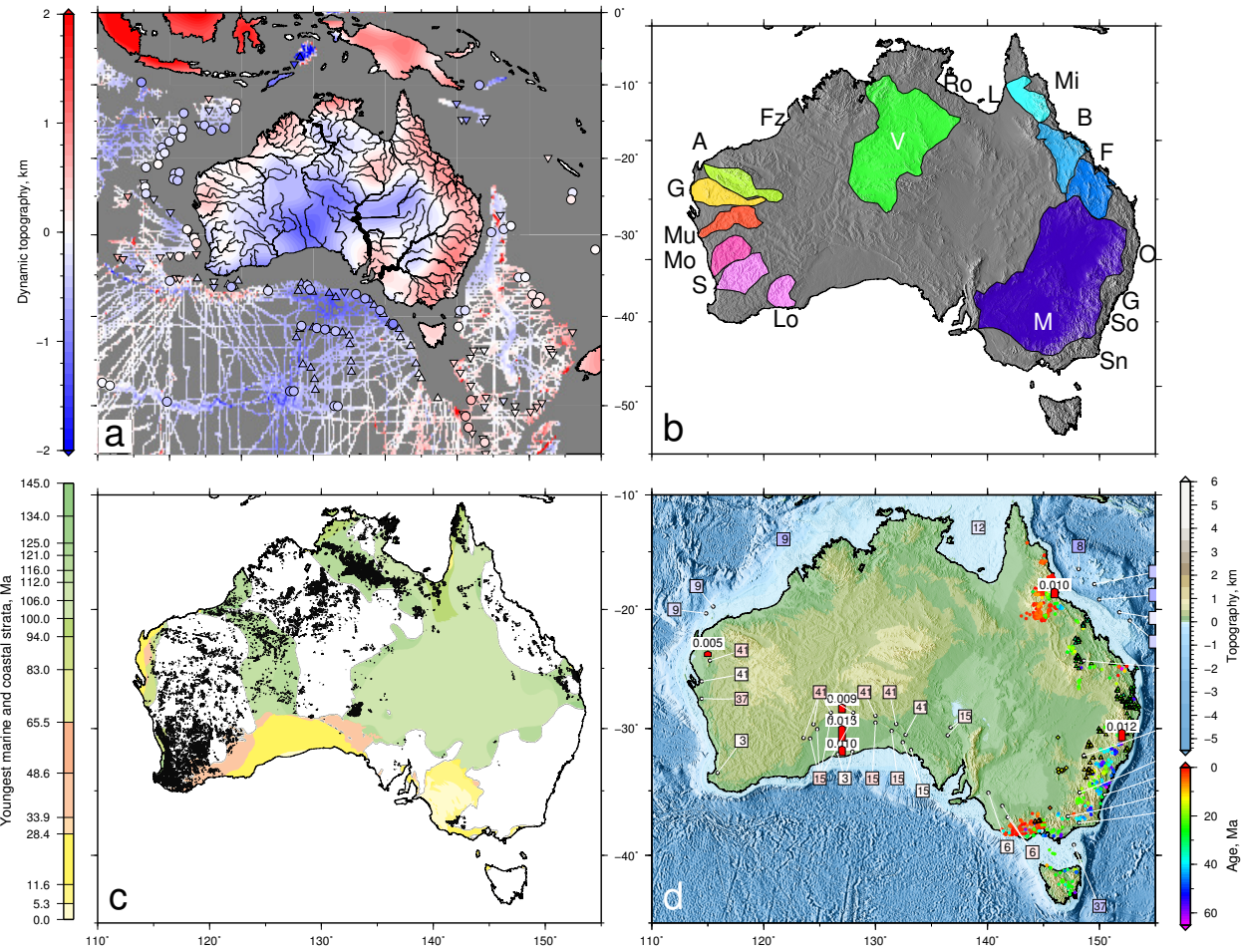**Figure 9.** Independent geologic constraints for Australia. (a) Present-day dynamic support. Red and blue pattern onshore = positive and negative long wavelength free-air gravity anomalies filtered to remove wavelengths < 800 km, at 10 mgal intervals; circles/triangles/filigree offshore = residual bathymetric measurements [*Winterbourne et al.*, 2014; *Czarnota et al.*, 2014]; black drainage network = 253 rivers extracted from SRTM dataset. (b) Major drainage basins. V = Victoria, Fz = Fitzroy, A = Ashburton/Robe, G = Greenough, Mu = Murchison, Mo = Moore, S = Swan, Lo = Lort/Brandy Creek, M = Murray-Darling, Sn = Snowy, So = Shoalhaven, G = Grose, O = Oban, F = Fitzroy, B = Burdekin, Mi = Mitchell, L = Leichhardt, R = Roper. (c) Colored polygons = youngest marine and coastal strata [*Langford et al.*, 1995]. Black circles = distribution of Mesozoic and Cenozoic laterite deposits [*Raymond et al.*, 2012]. (d) Circles/triangles = mafic/bimodal magmatism; squares = regional uplift where color and number indicate magnitude and age in Ma [*Czarnota et al.*, 2014]. Numbered red arrows = uplift rates from emergent marine terraces where height is proportional to rate in mm/a [*Wellman*, 1987; *Langford et al.*, 1995; *Haig & Mory*, 2003; *Sandiford*, 2007].
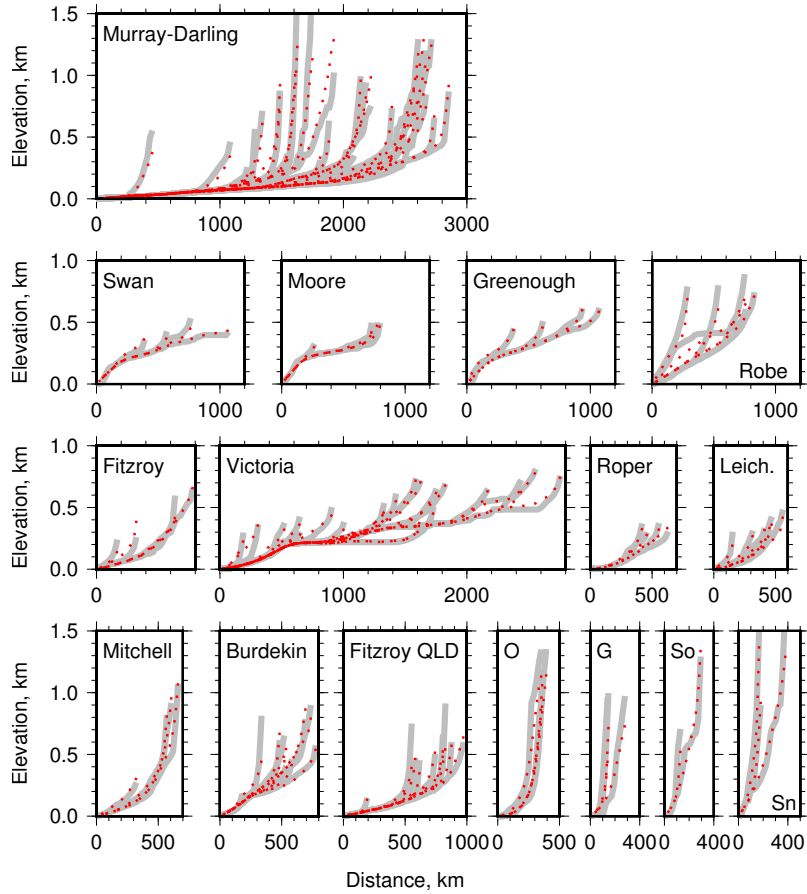
Figure 10. Inverse modeling of Australian river profiles arranged by catchment. Gray lines = observed river profiles; red dotted lines = best-fit theoretical river profiles generated using uplift history shown in Figure 11a; rms misfit = 1.8. Four lower right panels: O = Oban; G = Grose, So = Shoalhaven, Sn = Snowy.
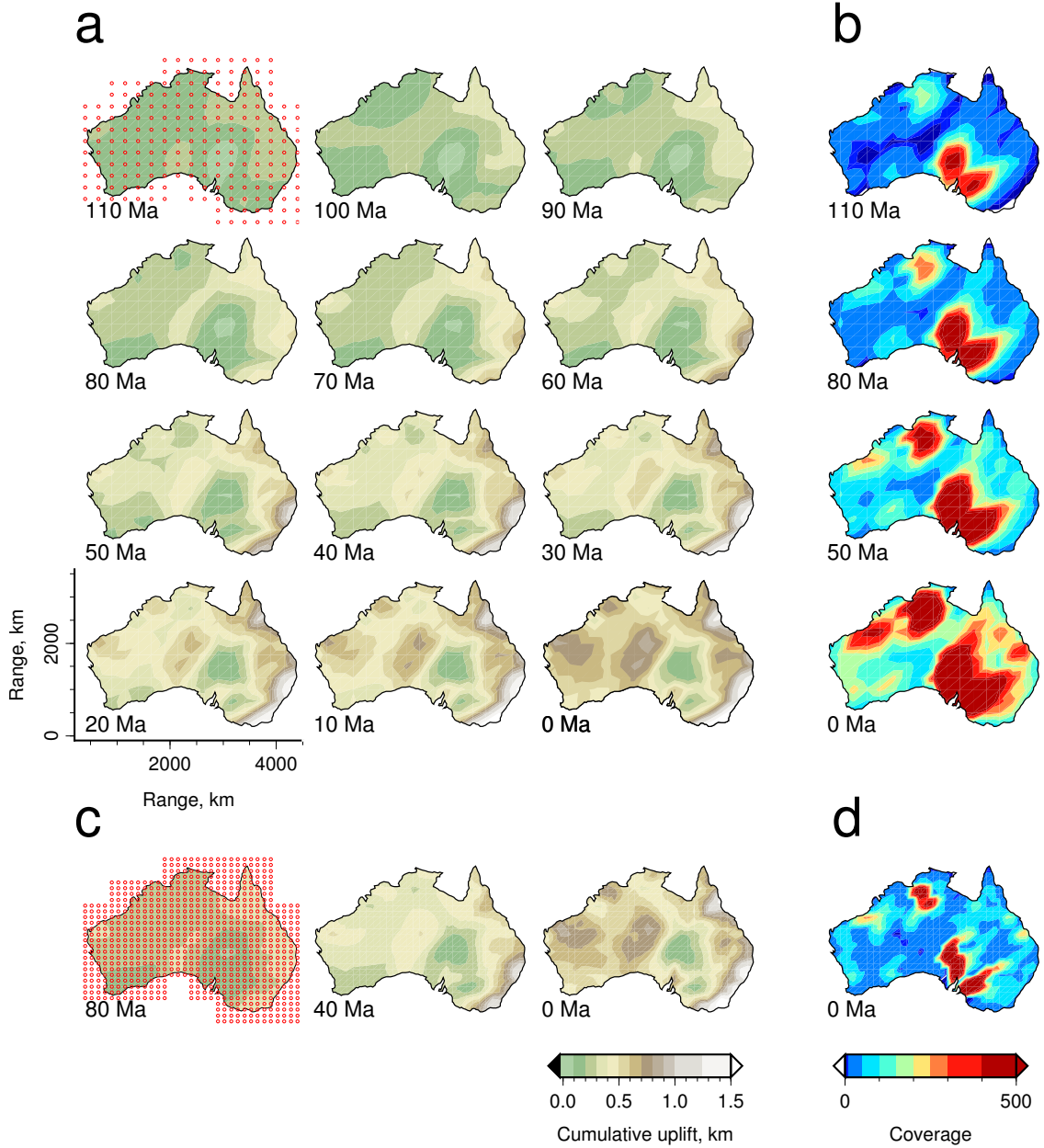
Figure 11. (a) Spatial and temporal pattern of cumulative uplift history for Australia from 110 Ma to present day at 10 Ma intervals. Red circles overlying top left-hand panel = spatial regularization grid where triangular mesh = ⊠. (b) Selected panels at four different times, which show number of non-zero entries in model matrix, M, corresponding to a given uplift node. (c) and (d) Inverse model with higher spatial resolution.
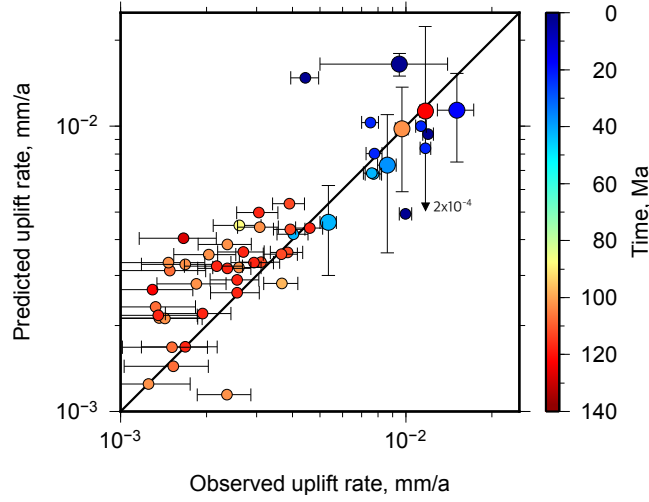
Figure 12. Comparison of observed and calculated uplift rates for Australia. Large circles = weighted mean values of uplift rate where color indicates age [Table 2; *Wellman*, 1987; *Langford et al.*, 1995; *Haig & Mory*, 2003; *Sandiford*, 2007]. Small circles with error bars = rates calculated from gridded heights and ages of uplifted marine deposits with uncertainties of 5×10^{-4} mm/a [*Langford et al.*, 1995; Figure 8c; Table 2]; vertical/horizontal lines with bars/arrows = uncertainties.
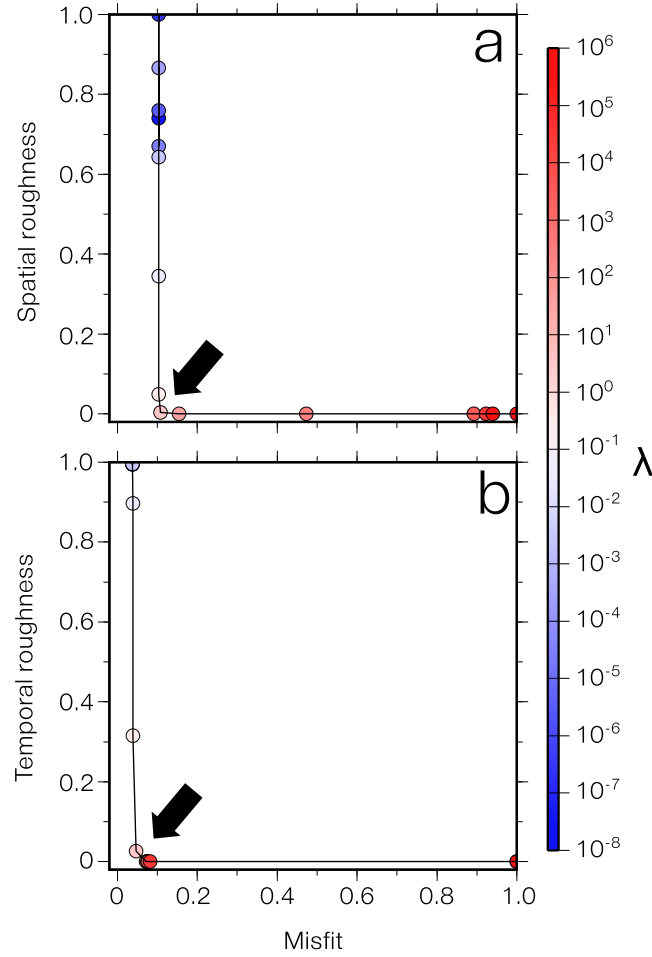
Figure 13. Model regularisation. (a) Normalized misfit as function of spatial smoothing for series of inverse models of 253 river profiles from Australia (see Figure 7 for misfit calculation). Colored circles = individual inverse models for different values of λ_S; black arrow = optimal inverse model. (b) Normalized misfit as function of temporal smoothing. Colored circles = individual inverse models for different values of λ_T.

	Locality	Latitude	Longitude	Age (Ma)	Elevation (m)	Uplift rate (mm/a)	Constraints
1	Pato's Kop	-33.34	27.37	44.85 ± 10.95	130	0.003 ± 0.001	a
2	Birbury	-33.19	27.62	44.85 ± 10.95	200	0.005 ± 0.001	a
3	Need's Camp	-33.09	27.73	44.85 ± 10.95	400	0.096 ± 0.002	a
	Weighted mean					$\mathbf{0.014 \pm 0.001}$	
	Predicted rate					$\mathbf{0.034 \pm 0.020}$	
4	S.W. of Maputo	-27.35	31.17	15.5 ± 5.5	900	0.057 ± 0.018	b, c
5	Durban	-30.02	29.52	15.5 ± 5.5	1150	0.073 ± 0.023	b, c
6	East London	-32.05	28.28	15.5 ± 5.5	1100	0.070 ± 0.022	b, c
7	E. of George	-33.76	22.48	15.5 ± 5.5	400	0.025 ± 0.008	b, c
	Weighted mean					$\mathbf{0.037 \pm 0.007}$	
	Predicted rate					$\mathbf{0.029 \pm 0.015}$	
8	S.W. of Maputo			3.57 ± 1.76	600	0.222 ± 0.109	b, c
9	Durban			3.57 ± 1.76	900	0.334 ± 0.165	b, c
10	East London			3.57 ± 1.76	850	0.314 ± 0.156	b, c
11	E. of George			3.57 ± 1.76	200	0.074 ± 0.036	b, c
12	Greenwood Park	-29.79	31.02	4.26 ± 0.68	65	0.016 ± 0.003	d
13	Bathurst	-33.74	26.46	4.47 ± 0.87	400	0.093 ± 0.018	b
	Weighted mean					$\mathbf{0.019 \pm 0.003}$	
	Predicted rate					$\mathbf{0.047 \pm 0.019}$	

Table 1. Observed and calculated uplift rates for South Africa.

	Locality	Latitude	Longitude	Age (Ma)	Elevation (m)	Uplift rate (mm/a)	Constraints
14	S. of P. Nolloth	-30.40	18.48	15.5 ± 5.5	250	0.016 ± 0.005	b, c
15	Saldanha bay	-32.99	17.96	13 ± 5	~ 150	0.020 ± 0.010	e
16	Hondeklip bay	-30.31	17.27	13 ± 5	~ 90	0.008 ± 0.003	e
	Weighted mean					**0.011 ± 0.002**	
	Predicted rate					**0.051 ± 0.029**	
17	S. of P. Nolloth	-30.40	18.48	3.57 ± 1.76	100	**0.037 ± 0.018**	b, c
	Predicted rate					**0.077 ± 0.077**	
18	Kuiseb R.	-23.34	15.74	1.6 ± 1.2	175 ± 75	**0.100 ± 0.060**	f
	Predicted rate					**0.074 ± 0.063**	
19	AN40-2	-15.20	12.13	0.133 ± 0.010	15	0.114 ± 0.010	g, h
20	AN57-1	-12.56	13.42	0.091 ± 0.006	11 ± 1	0.120 ± 0.020	g, h
21	AN27	-12.56	13.42	0.071 ± 0.007	28 ± 3	0.390 ± 0.080	g, h
22	AN47	-12.56	13.42	0.036 ± 0.003	9 ± 1	0.250 ± 0.050	g, h
	Weighted mean					**0.123 ± 0.009**	
	Predicted rate					**0.124 ± 0.062**	

Table 1. Continued. Observed and calculated uplift rates for West Africa.

	Locality	Latitude	Longitude	Age (Ma)	Elevation (m)	Uplift rate (mm/a)	Constraints
23	Tafoli	18.82	-15.05	0.099 ± 0.016	5 ± 1	0.054 ± 0.019	i
24	Tafoli	18.82	-15.05	0.258 ± 0.014	8 ± 2	0.032 ± 0.011	i
25	Tin Oueich	18.05	-15.83	0.122 ± 0.005	5 ± 1	0.041 ± 0.099	i
26	Tin Oueich	18.05	-15.83	0.241 ± 0.015	8 ± 2	0.034 ± 0.010	i
	Weighted mean					**0.036 ± 0.007**	
	Predicted rate					**0.036 ± 0.018**	
27	Agadir	30.52	-9.69	$0.115^{+0.075}_{-0.07}$	18 ± 0.5	**0.160 ± 0.010**	j
	Predicted rate					**0.287 ± 0.286**	
28	Somaâ	36.54	10.78	0.45 ± 0.113	96 ± 2	0.240 ± 0.110	k
29	Somaâ	36.54	10.78	0.27 ± 0.029	54 ± 4	0.200 ± 0.040	k
30	Somaâ	36.54	10.78	~ 0.123	23 ± 17	0.190 ± 0.140	k
	Weighted mean					**0.204 ± 0.036**	
	Predicted rate					**0.091 ± 0.053**	
31	Similani	-4.29	39.58	$0.0265^{+0.0013}_{-0.0015}$	4 ± 2	**0.160 ± 0.090**	l, m
	Predicted rate					**0.214 ± 0.214**	

Table 1.   Continued.   Observed and predicted uplift rates from North and East Africa.

[a]*Partridge & Maud* [1987] & [b]*Partridge* [1998]: biostratigraphic dating of marine terraces and correlation with warped peneplains; [c]*Partridge & Maud* [2000]: biostratigraphic dating of river incision and ^{40}Ar/^{39}Ar dating of pedogenic rock; [d]*Erlanger et al.* [2012]: ^{26}Al and ^{10}Be dating of marine terrace; [e]*Roberts & Brink* [2002]: biostratigraphic dating of strandlines; [f] *Van der Wateren & Dunai* [2001]: ^{21}Ne dating of fluvial incision rate between 2.8–0.4 Ma; [g]*Giresse et al.* [1984] & [h]*Guiraud et al.* [2010]: ^{230}Th/^{234}U, ^{231}Pa/^{231}U & ^{14}C dating of marine terraces; [i]*Giresse et al.* [2000]: U/Th dating of marine terraces; [j]*Meghraoui et al.* [1998]: U-Th dating of marine terraces; [k]*Elmejdoub & Jedoui* [2009]: OIS correlation of marine terraces, with U-series calibration from *Jedoui et al.* [2003]; [l]*Hori* [1970] & [m]*Odada* [1996]: ^{14}C dating of marine terraces.

	Locality	Latitude	Longitude	Age (Ma)	Elevation (m)	Uplift rate (mm/a)	Constraints
32	Nullabor	-28.70	127.00	~ 36	310 ± 23	$\mathbf{0.0086 \pm 0.0006}$	n
	Predicted rate					$\mathbf{0.0073 \pm 0.0037}$	
33	Nullabor	-31.00	127.00	~ 15	227 ± 34	$\mathbf{0.0151 \pm 0.0022}$	n
	Predicted rate					$\mathbf{0.0114 \pm 0.0039}$	
34	Nullabor	-32.20	127.00	~ 3	23 ± 8	$\mathbf{0.0095 \pm 0.0045}$	n
	Predicted rate					$\mathbf{0.0165 \pm 0.0015}$	
35	Pilbara	-24.00	115.00	39 ± 2	~ 190	$\mathbf{0.0054 \pm 0.0045}$	o
	Predicted rate					$\mathbf{0.0046 \pm 0.0016}$	
36	MacLeay R.	-31.00	152.00	120 ± 5	~ 1400	$\mathbf{0.0117 \pm 0.0005}$	p, q
	Predicted rate					$\mathbf{0.0113 \pm 0.0111}$	
37	Herbert R.	-19.00	146.00	103 ± 5	~ 1000	$\mathbf{0.0098 \pm 0.0005}$	p, q
	Predicted rate					$\mathbf{0.0091 \pm 0.0039}$	

Table 2. Observed and predicted uplift rates in Australia. [n]*Sandiford* [2007]: uplifted marine terraces; [o]*Haig & Mory* [2003]: Marine sedimentary rocks; [p]*Wellman* [1987] & [q]*Langford et al.* [1995]: Youngest marine deposits.

Symbol	Description	Value	Units
z	Elevation		m
x	Distance along river		m
A	Upstream drainage area		m^2
t	Time		Ma
τ_G	Gilbert time		Ma
U	Uplift rate		mm a^{-1}
v	Advective coefficient of erosion	3.5–200	m^{1-2m} Ma^{-1}
$v_\circ$	Advective coefficient of erosion	0.5–25	m^{1-3m} Ma^{m-1}
m	Erosional constant	0.2–0.35	dimensionless
κ	Diffusivity	1–10^7	m^2 Ma^{-1}

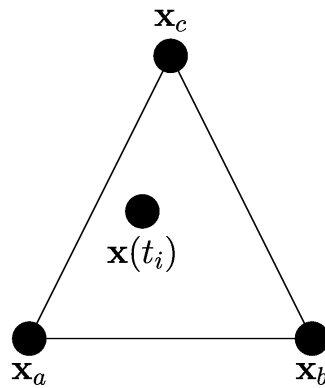**Table 3.** Parameters used for inverse modeling.

Figure 14. Barycentric coordinates $\mathbf{x}(t_i) = \alpha\mathbf{x}_a + \beta\mathbf{x}_b + \gamma\mathbf{x}_c$ where $\alpha + \beta + \gamma = 1$.
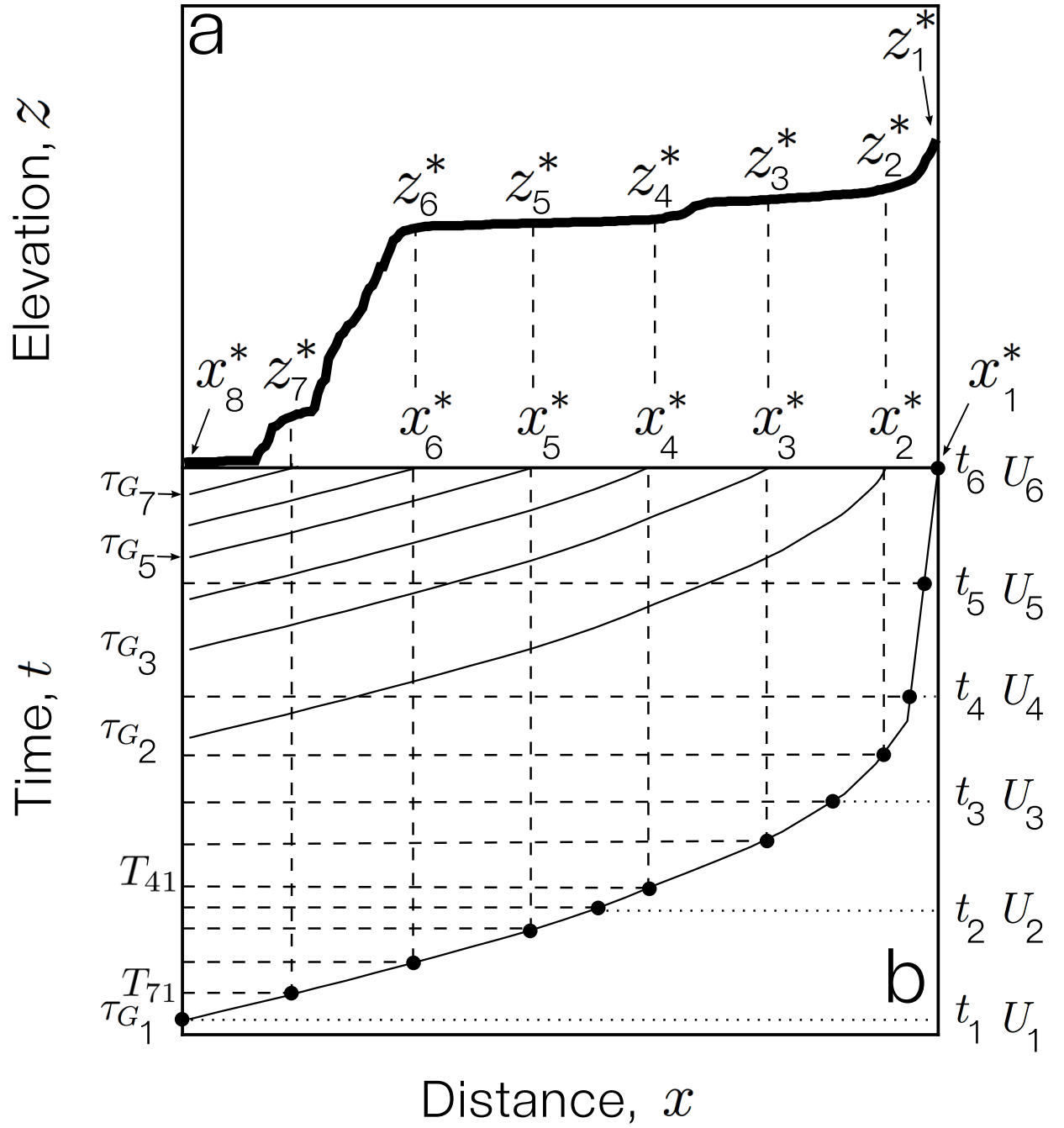
Figure 15. Diagram showing characteristic paths and notation for Ngunza river profile, Bié dome, West Africa.